DOI: https://doi.org/10.2138/am-2021-7626. http://www.minsocam.org/

REVISION 1

Stable and Transient Isotopic Trends in the Crustal Evolution of Zealandia Cordillera

Joshua J. Schwartz[1], Solishia Andico[1], Rose Turnbull[2], Keith A. Klepeis[3], Andy Tulloch[2], Kouki Kitajima[4], and John W. Valley[4]

[1] *Department of Geology, California State University Northridge, CA, 91330, USA*
[2] *GNS Science, Private Bag 1930, Dunedin, NZ*
[3] *Department of Geology, The University of Vermont, VT, 05405, USA*
[4] *WiscSIMS, Dept. of Geoscience, University of Wisconsin, Madison, WI 53706, USA*
* corresponding author: email: joshua.schwartz@csun.edu; tel. (818) 677-5813

ABSTRACT (352/800 words)

We present >500 zircon $\delta^{18}O$ and Lu-Hf isotope analyses on previously dated zircons to explore the interplay between spatial and temporal magmatic signals in Zealandia Cordillera. Our data cover ~8,500 km^2 of middle and lower crust in the Median Batholith (Fiordland segment of Zealandia Cordillera) where Mesozoic arc magmatism along the paleo-Pacific margin of Gondwana was focused along an ~100 km-wide, arc-parallel zone. Our data reveal three spatially distinct isotope domains which we term the eastern, central and western isotope domains. These domains parallel the Mesozoic arc-axis and their boundaries are defined by major crustal-scale faults that were reactivated as ductile shear zones during the Early Cretaceous. The western isotope domain has homogenous, mantle-like $\delta^{18}O$ (Zrn) values of 5.8 ± 0.3‰ (2SD) and initial ε_{Hf} (Zrn) values of +4.2 ±

1.0 (2SD). The eastern isotope domain is defined by isotopically low and homogenous $\delta^{18}O$ (Zrn) values of 3.9 ± 0.2‰ and initial ε_{Hf} values of +7.8 ± 0.6. The central isotope domain is characterized by transitional isotope values that display a strong E-W gradient with $\delta^{18}O$ (Zrn) values rising from 4.6‰ to 5.9‰ and initial ε_{Hf} values decreasing from +5.5 to +3.7. We find that the isotope architecture of the Median Batholith was in place before initiation of Mesozoic arc magmatism and pre-dates Early Cretaceous contractional deformation and transpression. Our data show that Mesozoic pluton chemistry was controlled in part by long-lived, spatially distinct isotope domains that extend from the crust through to the upper mantle. Isotope differences between these domains are the result of the crustal architecture (an underthrusted low-$\delta^{18}O$ source terrane) and a transient event beginning at ca. 129 Ma that primarily involved a depleted-mantle component contaminated by recycled trench sediments (10-20%). When data showing the temporal and spatial patterns of magmatism are integrated, we observe a pattern of decreasing crustal recycling of the low-$\delta^{18}O$ source over time, which ultimately culminated in a mantle-controlled flare-up. Our data demonstrate that spatial and temporal signals are intimately linked and when evaluated together they provide important insights into crustal architecture and the role of both stable and transient arc magmatic trends in Cordilleran batholiths.

Keywords: Cordilleran magmatism, Zealandia, zircon, O isotopes, Hf isotopes

for submission to *American Mineralogist John Valley Volume*

Introduction

The crustal architecture of continental margins plays an important role in influencing the location of Cordilleran-arc magmatism and the geochemical and isotope evolution of arc magmas from their source to emplacement (e.g., Ducea et al., 2015a). Geochemical and isotope data from arc magmas are often used as important features in evaluating source regions and differentiation processes that ultimately lead to the generation of continental crust through time (Rudnick, 1995; Taylor and McLennan, 1995; Ducea and Barton, 2007; Scholl and von Huene, 2007; Hawkesworth et al., 2010; Voice et al., 2011; Ducea et al., 2017). However, the record of pre-existing crustal sources and their relationship to terrane and intra-terrane faults is commonly highly disrupted by a variety of factors including voluminous magmatic intrusions, polyphase metamorphism, and various phases of brittle and ductile faulting. The end result is that surficial exposures of long-lived Cordilleran arcs preserve an incomplete record of crustal sources and the pre-batholithic architecture of the arc which were once key factors in its temporal and spatial magmatic evolution.

One of the problems in understanding isotope variations in arc magmas is that isotope signals can be influenced by a number of competing factors, including spatially controlled features such as the crustal and upper mantle architecture and composition of the arc (Armstrong, 1988; Ducea and Barton, 2007), versus various transient tectonic and non-tectonic processes that can introduce new sources. The latter may include processes such as delamination and arc root foundering (Kay et al., 1994; Ducea, 2002; Ducea et al., 2013), fore-arc underplating (Chapman et al., 2013), subduction erosion (Kay et al., 2005), retro-arc underthrusting of continental crust (DeCelles et al., 2009; DeCelles and Graham, 2015), relamination of subducted sediment (Hacker et al., 2011), and/or slab tears and slab windows (Thorkelson, 1996; Dickenson, 1997).

Understanding which of these mechanisms controls geochemical and isotope changes in arc magma chemistry is critical in evaluating continental crustal growth processes, including triggering mechanisms for voluminous arc magmatic surges (Paterson and Ducea, 2015; Ducea et al., 2015b; de Silva et al., 2015).

The Mesozoic Median Batholith of Fiordland New Zealand is a prime location to explore the interplay between spatial- and temporal-isotope signals because it comprises ~10,000 km^2 of lower, middle and shallow arc crust built on the southeast margin of Gondwana from the Devonian to Early Cretaceous (**Fig. 1A-F**) (Landis and Coombs, 1967; Mortimer et al., 1999a; Tulloch and Kimbrough, 2003). The importance of the Median Batholith in understanding Cordilleran-arc magmatic processes is underscored by competing models for the Early Cretaceous surge of high-Sr/Y magmatism. In one model, Muir et al. (1995) and Milan et al. (2017) used bulk-rock and zircon radiogenic isotope data (Sr-Nd-Hf) to argue for increasing contributions of ancient (radiogenic) continental crustal sources during the continentward advance of the arc. In contrast, Decker et al. (2017) used both stable and radiogenic zircon isotope data (O and Lu-Hf) from the lower crust of the Median Batholith to propose a mantle (rather than crustal) trigger for the Early Cretaceous flare-up stage. In neither study were spatial isotope trends investigated nor was the role of the pre-existing crustal architecture considered. Consequently, an outstanding question is whether geochemical and isotope shifts observed in magmatic chemistry in the Mesozoic portion of the Median Batholith reflect temporally transient arc processes (c.f., increased coupling, underthrusting of continental crust, and changes to the lower plate), or temporally stable processes influenced by long-lived pre-batholithic crustal and/or upper lithospheric mantle architecture of the Cordilleran arc system. In the Median Batholith, this problem is compounded by the fact that there is little consensus about the pre-

This is the peer-reviewed, final accepted version for American Mineralogist, published by the Mineralogical Society of America.
The published version is subject to change. Cite as Authors (Year) Title. American Mineralogist, in press.
DOI: https://doi.org/10.2138/am-2021-7626. http://www.minsocam.org/

batholithic crustal architecture, the nature and location of isotope boundaries, nor the timing of terrane juxtaposition prior to voluminous arc-magmatic activity in the Early Cretaceous (Kimbrough et al., 1994; Adams et al., 1998; Muir et al., 1998; Mortimer et al., 1999a; Scott et al., 2009; McCoy-West et al., 2014).

Zircon isotope studies in plutonic rocks can improve our understanding of the crustal architecture and spatial isotope trends prior to batholith emplacement because they can reveal differences in source regions from which melts were derived (e.g., Valley, 2003; Lackey et al., 2005; Lackey et al., 2008; Cecil et al., 2011; Lackey et al., 2012). For example, oxygen isotopes are particularly sensitive indicators of melt-rock interaction and differentiate low-temperature hydrothermally altered sources, such as marine sediments ($\delta^{18}0 >>6‰$), from high-temperature hydrothermally altered sources or those altered at high paleo-latitude or -altitude conditions ($\delta^{18}O <<6‰$). Similarly, hafnium isotopes differentiate depleted mantle-derived melts (and/or reworked mantle-derived protoliths: ε_{Hf} = +16 to +18) from older crustal sources (initial ε_{Hf} << +16). Moreover, variations in zircon isotope values within samples also provide information about whether isotope signatures were acquired from deep-crustal source regions versus during ascent or at the depth of emplacement. Isotope signatures acquired in the deep crust or upper mantle often display homogenous values with low intrasample standard deviations reflecting efficient isotope homogenization in high-temperature melt-rich systems, whereas large intrasample variations can be caused by assimilation of crustal sources during ascent, remelting of sedimentary protoliths, or emplacement in melt-poor, crystal mushes (e.g., Valley et al., 1998; Kemp et al., 2007; Miller et al., 2007; Bindeman, 2008). In this study, we use a series ~60-km long, arc-perpendicular zircon isotope transects from Jurassic to Early Cretaceous plutons to investigate the isotope characteristics of the Median Batholith with the goal of understanding the pre-batholithic crustal architecture and evaluating temporal and spatial isotope variations in Cordilleran crust construction in the Zealandia Cordillera (**Fig. 1**).

Geologic Background

Regional Geology of the Median Batholith

Currently exposed Pre-Late Cretaceous Zealandia is divided into two lithologic provinces: the Eastern Province and the Western Province (**Fig. 1A-B, F**). The Eastern Province consists of dominantly Permian to Early Cretaceous accreted terranes composed of sedimentary and metasedimentary terranes (Murihiku, Caples, Torlesse, Waipapa Terranes, and Haast Schist), an ophiolite belt (Dun Mountain/Maitai Terrane), and an intraoceanic island arc terrane (Brook Street Terrane) (Landis and Coombs, 1967; Frost and Coombs, 1989; Bradshaw, 1993; Mortimer et al., 1999a; Tulloch et al., 1999a; Mortimer, 2004; Campbell et al., 2020).

The Western Province is comprised of Early Paleozoic Gondwana-like affinity metasedimentary and metavolcanic rocks comprising Buller and Takaka terranes that were accreted to the Gondwana margin in the Early Paleozoic (Cooper and Tulloch, 1992, Jongens, 1997; 2006) and intruded by Ordovician to Cretaceous plutons (Mortimer et al. 2004; Ramezani and Tulloch, 2009; Tulloch et al. 2009a) (**Fig. 1A-B**). While the boundary between the Eastern Province and Western Provinces is generally thought to lie between the Brook Street Terrane and the Takaka/Buller terranes, the region is overprinted by Cenozoic brittle faults and Mesozoic plutons of the Median Batholith (**Fig. 1A-B**). Thus, there is no consensus on the location of the boundary between the Eastern Province and Western Provinces nor the timing of its formation. We investigate the architecture of this boundary in this contribution because it forms the background for understanding spatial and temporal isotope trends in the Median Batholith.

DOI: https://doi.org/10.2138/am-2021-7626. http://www.minsocam.org/

Mortimer et al. (1999) recognized that the boundary between the Eastern and Western Provinces is essentially defined by variably deformed batholithic rocks and they coined the term 'Median Batholith' to describe the region where batholithic rocks intrude both Western Province and Eastern Province terranes (**Fig. 1**). Tulloch and Kimbrough (2003) subsequently subdivided the Median Batholith into two overlapping plutonic belts (the inboard and outboard belts) which contain the Darran and the Separation Point Suites (**Fig. 1**). Recognition of correlative rocks in off-shore South Zealandia indicates that the Median Batholith extends along at least 2600km of the SE Gondwana margin (Tulloch et al. 2019). In the deeply exhumed 200km long segment of the Median Batholith in Fiordland, the inboard belt is dominated by the monzodioritic Western Fiordland Orthogneiss (WFO) phase of the Separation Point Suite (Oliver 1977; Mattinson et al 1986; Bradshaw 1990). The WFO was emplaced in the lower crust and in part metamorphosed to granulite facies, in marked contrast to the upper/mid-crustal plutonic and rare volcanic rocks of the Darran Suite that dominate the outboard belt (**Fig. 1; Table 1**).

The boundary between the inboard and outboard belts was defined by Allibone et al. (2009) by the distribution of metasedimentary rocks, whereby those of the inboard belt have Gondwana-affinities, and those in the outboard Median Batholith have no apparent association with cratonic Gondwana. In northern Fiordland, Marcotte et al. (2005) suggested that the Indecision Creek Shear Zone represented the boundary between the inboard and outboard Median Batholith, and Scott et al. (2009) suggested that this boundary continued to the south to the subvertical Grebe Shear Zone in Lake Manapouri in central Fiordland (**Fig. 1A**). Buriticá et al. (2019) extended the Grebe Shear Zone into South Fiord, Lake Te Anau and noted that deformation is partitioned into a diffuse network of high- and low-strain mylonitic shear zones whose core deformation zone is located within the Darran Suite. We use the location of the

Grebe and Indecision Creek Shear Zones as defined in these prior studies as the boundary between inboard and outboard plutons rocks in this study.

In a re-evaluation of the inboard/outboard concept, Scott (2013) subdivided the Median Batholith by terranes whereby rocks east of the Grebe Shear Zone-Indecision Creek Shear Zone are considered part of the Drumduan Terrane, and rocks west of the Grebe Shear Zone-Indecision Creek Shear Zone are considered part of the Takaka Terrane (**Fig. 1A, F**). These subdivisions are illustrated in **Table 1** and in **Fig. 1A** along with the isotope domains that we introduce later. For the sake of simplicity, we continue to use the terms 'inboard' and 'outboard' Median Batholith to describe plutonic rocks relative to the Grebe Shear Zone-Indecision Creek Shear Zone because these terms are ingrained in the literature.

Previous Isotope Studies of the Median Batholith

The inboard Median Batholith consists of Mesozoic plutons including the Western Fiordland Orthogneiss, and parts of Separation Point Suite and Darran Suite (**Fig. 1A**) Kimbrough et al., 1994; Gibson and Ireland, 1996; Scott and Palin, 2008; Allibone et al., 2009a, 2009b; Milan et al., 2016; Milan et al., 2017; Decker et al., 2017; Schwartz et al., 2017; Buriticá et al., 2019). Only the Western Fiordland Orthogneiss in the inboard Median Batholith has been investigated isotopically in detail. It has $\delta^{18}O$ (Zrn) values ranging from 5.2 to 6.3‰ and initial ε_{Hf} (Zrn) values ranging from -2.0 to +11.2 (Bolhar et al., 2008; Milan et al., 2016; Decker et al., 2017). Western Fiordland Orthogneiss plutonic rocks have bulk-rock initial $^{87}Sr/^{86}Sr$ values of 0.70391 ± 4, and initial ε_{Nd} values ranging from -0.4 to +2.7 (McCulloch et al., 1987).

The outboard Median Batholith was defined by Tulloch and Kimbrough (2003) by the presence of Triassic to Cretaceous Darran Suite (235-132 Ma) and also includes some Separation

Point Suite rocks (125-122 Ma) (Kimbrough et al., 1994; Muir et al., 1998; Tulloch and Kimbrough, 2003; Bolhar et al., 2008; Scott and Palin, 2008; Allibone et al., 2009b; Scott et al., 2009; Buriticá et al., 2019). There are no $\delta^{18}O$ (Zrn) data for the outboard Darran Suite; however, Scott et al., (2009) report initial ε_{Hf} (Zrn) values of +5.9 to +10.0 from 2 samples, and McCulloch et al. (1987) report bulk-rock initial $^{87}Sr/^{86}Sr$ values from 0.70373 and 0.70387 and initial ε_{Nd} values between +3.9 to +4.6. From the Separation Point Suite, Bolhar et al. (2008) report 3 samples that have $\delta^{18}O$ (Zrn) values of 3.1 to 4.4‰ and initial ε_{Hf} (Zrn) values of +7.4 to +8.3. Muir et al. (1998) also report two bulk-rock initial $^{87}Sr/^{86}Sr$ values from the same samples which range from 0.70375-0.70377 and have initial ε_{Nd} values of +3.2.

Methods

Bulk-rock geochemistry

Bulk-rock samples were powdered in an alumina ceramic shatter-box. Powders were mixed with a 2:1 ratio of SpectroMelt A10 lithium tetra borate flux and melted at 1000°C for approximately 20 minutes to create glass beads at California State University, Northridge. Beads were repowdered, refused following the initial melting parameters, and polished to remove carbon from the flat bottom where analysis occurs. Following procedures outlined in Lackey et al. (2012), glass beads were analyzed at Pomona College for major (SiO_2, TiO_2, Al_2O_3, Fe_2O_3, MnO, MgO, CaO, Na_2O, K_2O, P_2O_5) and trace (Rb, Sr, Ba, Zr, Y, Nb, Cs, Sc, V, Cr, Ni, Cu, Zn, Ga, La, Ce, Pr, Nd, Hf, Pb, Th, U) elements by X-ray fluorescence (XRF). Beads were analyzed with a 3.0kW Panalytical Axios wavelength-dispersive XRF spectrometer with PX1, GE, LiF 220, LiF 200, and PE analyzer crystals. Bulk-rock geochemistry values are shown in **Figure 2** and reported in Supplemental Table 1.

Zircon separation

Zircons were extracted from rock samples at the CSUN rock lab following methods in Schwartz et al. (2017). Zircons without visible inclusions were hand-picked and placed onto double sided tape with zircon standards. The KIM-5 zircon standard ($\delta^{18}O$ = 5.09 +- 0.06‰ VSMOW, Valley 2003) was mounted near the center of each mount for oxygen isotope analysis. Zircons were imaged in epoxy mounts using a Gatan MiniCL cathodoluminescence detector on a FEI Quanta 600 Scanning Electron Microscope at CSUN (**Fig. 3**). U-Pb zircon geochronology data were collected by Secondary Ion Mass Spectrometry at the Stanford-USGS Sensitive High Resolution Ion Microprobe – Reverse Geometry (SHRIMP-RG) facility. These age data are reported in Buriticá et al. (2019) and geochronology data are summarized in **Table 2**.

Zircon Oxygen Isotopes

Zircon oxygen isotope analyses were conducted at the University of Wisconsin-Madison WiscSIMS lab using a CAMECA IMS 1280 ion microprobe, following procedures from Kita et al. (2009). CL and reflected light imaging were conducted on mounts after U-Pb analyses to select locations (from the same magmatic domain) for O analysis. Zircon mounts were polished with a 6, 3, and 1 μm diamond lapping film to remove U-Pb spots collected prior to O-isotope analyses. Where zircons maintained a U-Pb pit, oxygen isotopes were collected in a different location within the same igneous domain to avoid contamination from the oxygen beam used during U-Pb analyses. Mounts were cleaned in ethanol and deionized water baths using an ultrasonic cleaner, dried in a vacuum oven, gold-coated, and stored in a de-gassing vacuum prior to secondary ion mass spectrometry (SIMS) analysis. A 10kV $^{133}Cs^{+}$ primary beam was used for analysis of ~10 µm spots. Oxygen isotopes ($^{18}O^{-}$, $^{16}O^{-}$) and $^{16}O^{1}H^{-}$ were collected in three Faraday cups. For each session, four KIM-5 zircon standards (Valley et al., 2003) were measured before and after analyzing 8 – 15 unknowns. Standardization was conducted on a bracket by bracket basis using the 8 KIM-5 standard analyses. Individual spot analysis precision for KIM-5 ranged from 0.09 – 0.25‰ (ave. = 0.17‰, 2SD) (Table 2). Values of $^{16}O^{1}H$ /^{16}O are corrected for background measured on bracketing KIM-5 and referred to as OH/O hereafter (Wang et al. 2014). After oxygen isotope analyses, mounts were imaged to verify igneous domains were analyzed at the University of California, Los Angeles using a Tescan Vega-3 XMU variable-pressure (VP) Scanning Electron Microscope (SEM) at 20kV and working distance of 20 mm with a cathodoluminescence detector. Values of $\delta^{18}O$ are reported in permil notation relative to V-SMOW (Supplementary Table 2) and summarized in **Table 2**. Representative zircons and sample spots are shown in **Figure 3**. Zircon oxygen isotope ratios relative to distance from the Grebe Shear Zone (GSZ) are plotted in **Figures 4 and 5**.

Zircon Lu-Hf Isotopes

Hafnium isotope analyses were collected at the Arizona LaserChron Center using a Nu Plasma multicollector ICPMS on individual zircon grains. Prior to analysis, gold coating on mounts and in SIMS pits from previous oxygen-isotope analysis was removed by polishing with 6, 3, and 1 µm diamond lapping film. Mounts were then immersed in a potassium iodine solution. When possible, Hf isotope analyses occurred on existing oxygen pits or similar igneous domains. Data were collected using a Nu Plasma HR ICP-MS, coupled to a New Wave 193 nm ArF laser ablation system equipped with a Photon Machines Analyte G2 laser equipped with a LelEX cell. The ICP-MS has 12 fixed Faraday detectors equipped with $3x10^{11}$ Ω resistors, 10 of

DOI: https://doi.org/10.2138/am-2021-7626. http://www.minsocam.org/

which are used to measure masses ^{171}Yb through ^{180}Hf. This resistor configuration is used to provide enhanced signal:noise for the low intensity ion beams generated by laser ablation. Hf-Yb-Lu solutions were introduced in Ar carrier gas via a Nu DSN-100 desolvating nebulizer with He carrier gas mixed with Ar make-up gas. The instrument was tuned with a 10 ppb solution of standard JMC475 (Vervoort et al., 2004). Analyses consisted of one zircon of each standard Mud Tank, FC52, SL, 91500, Temora, Plesovice, and R33, followed by 10 unknowns (see **Supplementary Figure 1** for standard data). For each analytical session, standards and unknowns were reduced together (**Supplementary Table 3**). A summary of isotope values is reported in **Table 2**. Representative zircons and sample spots are shown in **Figure 3**. Zircon initial εHf values relative to distance from the Grebe Shear Zone are plotted in **Figures 4 and 5**.

Isotope Contour Plots

Isotope contour plots were created by importing latitude, longitude, and isotope values of each sample into Surfer™ 11 using a minimum curvature gridding method. Oxygen and hafnium isotope contour plots of Fiordland were constructed with a latitude range of S 45°8’00.0” to E 44°4’00.0” and longitude range of 166°4’00.0” to 168°2’00.0”, and plots were clipped to the shape of Fiordland using Adobe Illustrator™ (**Fig. 6**). The oxygen isotope contour plot has a contour interval of 0.3‰ to encompass the average 2SD precision (0.17‰) for the entire data set, and the hafnium isotope contour plot has a contour interval of 1.0 ε unit to encompass the average 2SD of 1.2 ε units. The oxygen contour plot of samples along Lake Te Anau and Lake Manapouri (locations shown in **Fig. 1**) are plotted with a contour interval of 0.4‰ in Figure 7A to encompass the average 2SD for these samples.

RESULTS

Bulk-Rock Geochemistry

The Western Fiordland Orthogneiss is dominantly monzodioritic in composition, metaluminous, alkali-calcic to calc-alkalic, and magnesian (red circles in **Fig. 2A-D**). It is also characterized by high-Sr/Y bulk-rock values (generally >40) and has moderate depletions in heavy rare earth elements in chondrite-normalized rare earth element plots (e.g., Decker et al., 2017). The Western Fiordland Orthogneiss is part of the more widely distributed high-Sr/Y Separation Point Suite (129-110 Ma) that is characterized by a broad range in SiO_2 ranging from 54-76% (Kimbrough et al., 1994; Muir et al., 1995; Tulloch and Kimbrough, 2003; Buriticá et al., 2019). Other inboard Separation Point Suite plutons are classified as monzodiorite to granite, and are dominantly metaluminous to peraluminous, alkali-calcic to calc-alkalic, and magnesian when SiO_2 wt.% is less than ~74 wt.% and ferroan when SiO_2 wt.% is greater than ~74 wt.% (orange circles in **Fig. 2A-D**). Inboard Darran Suite samples analyzed in this study are Middle to Late Jurassic in age and display a broad range in SiO_2 wt.% from 49 to 69 wt.% (**Table 2**; grey circles in **Fig. 2A-D**). Darran Suite rocks are classified as monzodiorite to granodiorite, metaluminous to peraluminous, alkali-calcic to calcic, and magnesian (**Fig. 2A-D**). In contrast to the inboard Separation Point Suite, rocks of the inboard Darran Suite have low Sr/Y values (generally <40; Tulloch and Kimbrough, 2003).

Outboard Separation Point Suite plutons are also classified as high Sr/Y but are distinguished from inboard Separation Point Suite plutonic rocks by a much more restricted range in SiO_2 (70-76 wt.%) particularly for the three large plutons shown in **Fig. 1A**. They are generally two-mica granites and are strongly peraluminous. They are also alkali-calcic to calc-alkalic, and magnesian (orange squares in **Fig. 2A-D**). Outboard Darran Suite plutonic rocks display broad range of SiO_2 wt.% from 50% to 76 wt.%. They are also classified as gabbro to granite, and they are metaluminous to peraluminous, alkali-calcic to calc-alkalic, and dominantly magnesian with several ferroan outliers at high SiO_2 values (grey squares in **Fig. 2A-D**). Like their inboard equivalent, outboard Darran Suite plutonic rocks are also low Sr/Y.

Zircon Oxygen Isotopes

Oxygen isotopes were analyzed from 34 samples collected along four ~60-km long, arc-perpendicular transects across the Median Batholith (**Fig. 1**). Samples include 10 samples from Western Fiordland Orthogneiss, 18 samples from Separation Point Suite, and 6 samples from Darran Suite. Zircon isotope data from all four transects shown in **Figures 4 and 5** include data from Decker et al. (2017) and display a strong isotope gradient with $\delta^{18}O$ (Zrn) values increasing from east to west. This gradient exists both within Darran Suite and Separation Point Suite plutons and across the Median Batholith (**Fig. 6**). Samples from Western Fiordland Orthogneiss located west of the George Sound Shear Zone have homogeneous, mantle-like values of 5.8 ± 0.3‰ (n=24; **Fig. 5A**), a feature also observed by Decker et al. (2017). Inboard Separation Point Suite and Darran Suite plutons located east of the George Sound Shear Zone and west of the Grebe Shear Zone–Indecision Creek Shear Zone show decreasing $\delta^{18}O$ values from west to east with $\delta^{18}O$ (Zrn) values decreasing from 5.9 to 4.6‰ and we observe a pronounced decrease in $\delta^{18}O$ (Zrn) values within ~10 km of the Grebe Shear Zone–Indecision Creek Shear Zone (**Fig. 5A**). Outboard Separation Point Suite and Darran Suite samples located east of the Grebe Shear Zone–Indecision Creek Shear Zone also have homogeneous values with a combined average value of 3.9 ± 0.2‰ (n=7; **Fig. 5A**). In the discussion section, we refer to $\delta^{18}O$ (Zrn) as 'mantle-

DOI: https://doi.org/10.2138/am-2021-7626. http://www.minsocam.org/

like' if they fall within the average high-temperature SIMS mantle zircon value (5.3± 0.8‰). In contrast, we refer to values as 'low-δ^{18}O' if they fall below the lower limit of the average high-temperature SIMS mantle zircon value of 4.5‰.

The geographic distribution of zircon ^{18}O values define three isotope domains: the Western Isotope Domain (WID) consisting of Western Fiordland Orthogneiss plutons with δ^{18}O (Zrn) values ranging from 5.3‰ to 6.1‰ (average = 5.8 ± 0.3‰); the Central Isotope Domain (CID) defined by inboard Separation Point Suite and Darran Suite plutons with δ^{18}O (Zrn) values increasing from 4.6‰ (east) to 5.9‰ (west); and the Eastern Isotope Domain (EID) defined by outboard Separation Point Suite and Darran Suite plutons with δ^{18}O (Zrn) values ranging from 3.7‰ to 4.1‰ (average = 3.9 ± 0.2‰). The WID and EID are defined by δ^{18}O (Zrn) values with low internal 2SD, whereas the CID is characterized by increasing δ^{18}O (Zrn) values from east to west. Geographically, the EID roughly corresponds to the outboard Median Batholith and the Drumduan Terrane, whereas the CID and WID are located within the inboard Median Batholith and the Takaka Terrane (**Table 1**) (Allibone et al., 2009a; Scott et al., 2009; Scott, 2013).

A characteristic feature of all zircons from a single hand sample is their isotope homogeneity, indicated by low intra-sample values of 1 standard deviations ranging from 0.12‰ to 0.44‰ (**Table 2**). For all zircons sampled from Darran Suite, Separation Point Suite, and Western Fiordland Orthogneiss, the average intra-sample 2SD uncertainty is 0.28‰. The average two standard deviation uncertainty for inboard and outboard plutonic suites from this study are as follows: 0.22‰ for Western Fiordland Orthogneiss, 0.17‰ for inboard Separation Point Suite, 0.20‰ for outboard Separation Point Suite, 0.13‰ for inboard Darran Suite plutons, and 0.12‰ for outboard Darran Suite plutons. Individual zircon oxygen standard deviation values can be found in **Supplemental Table 3**.

DOI: https://doi.org/10.2138/am-2021-7626. http://www.minsocam.org/

Zircon Lu-Hf Isotopes

Zircon hafnium isotopes were analyzed for 19 samples and compiled with data from Decker et al. (2017) (**Figs. 4 and 5**). New analyses include two samples from Western Fiordland Orthogneiss, 13 samples from the Separation Point Suite, and 4 samples from the Darran Suite. Zircon initial ε_{Hf} data also display an isotope gradient increasing from west to east on both an intrapluton and regional scale (**Figs. 4-6**). Western Fiordland Orthogneiss plutons (WID) have nearly homogenous values of +4.2 ± 1.0 (2SD), inboard Separation Point Suite and Darran Suite plutons have an increasing west-east initial ε_{Hf} gradient of +4.0 to +5.5 (CID), and outboard Separation Point Suite and Darran Suite plutons have homogenous initial ε_{Hf} values of +7.8 ± 0.6 (EID) (**Fig. 5B**). Similar to $\delta^{18}O$ (Zrn) data above, zircon Hf isotope data also show a strong inflection within 10 km of the Grebe Shear Zone–Indecision Creek Shear Zone (**Fig. 5B**).

Isotope homogeneity is also prevalent in all samples across the Median Batholith, defined by low intra-sample standard deviations ranging from 0.5 (17NZ124A) to 2.5 ε units (17NZ140) (**Table 2**). The average 2SD precision for all zircons from inboard and outboard Darran Suite, Separation Point Suite, and Western Fiordland Orthogneiss is 1.2 ε units. From each plutonic suite, the average 2SD is as follows: 1.2 for Western Fiordland Orthogneiss, 1.2 for inboard Separation Point Suite, 1.2 for outboard Separation Point Suite, 1.6 for inboard Darran Suite, and 1.6 for outboard Darran Suite. Individual zircon standard deviation values can be found in Supplemental Table 3.

Discussion

Crustal and Isotope Architecture of the Median Batholith

Understanding the crustal and mantle structure of a Cordilleran margin is the first step in evaluating spatial and temporal isotope trends through time because the underlying crust/upper mantle plays a key role in influencing magma chemistry. In the case of the Median Batholith, much of the pre-Mesozoic architecture has been intruded by large Triassic to Cretaceous plutons, and this makes reconstructing the crustal architecture challenging. Ambiguities in the geology of this region have led to various attempts to understand this complex region and this has produced complex and oftentimes confusing terminology (**Table 1**). Our zircon O- and Hf-isotope data shed light on this problem by revealing the presence of three distinct arc-parallel isotope domains (EID, CID, WID). This information allows us to resolve a long-standing debate about the crustal structure of the Median Batholith including the relationship between the Eastern and Western provinces and the significance of shear zones as long-lived zones of lithospheric weakness and reactivation (Klepeis et al., 2019a,b).

A key finding in our data is that zircons in both the EID and WID have uniform O- and Hf- isotope values; however, zircons in the CID are characterized by transitional isotope values that lie between EID and WID end member values (**Fig. 5A-B**). This is particularly the case for $\delta^{18}O$ (Zrn) which appears to be a sensitive indicator of isotope differences within the Median Batholith (**Fig. 5A**). The transitional isotope domain (CID) lies within the inboard Median Batholith and the Takaka Terrane (Scott et al., 2009; Scott, 2013), and shares characteristics of both the EID and WID sources. In central Fiordland, the CID is a 20-km wide, arc-parallel zone of transpressional deformation that includes a number of highly elongate, syn-deformational Cretaceous plutons (e.g., Puteketeke, Refrigerator Orthogneiss, West Arm Leucogranite) and a series of mylonitic shear zones that were active during the Early Cretaceous flare-up (Scott et al., 2009; Buriticá et al., 2019; McGinn et al., 2020). The CID has not been previously recognized as a unique geochemical component of the Median Batholith; however, our data indicate that it is distinct from other parts of the batholith to the east and west as it displays transitional features and is bounded by major ductile shear zones on each side. The CID is also distinguished by the presence of a strong low-$\delta^{18}O$ signal which is strongest in the east and progressively decreases to the west where it becomes non-existent in the WID (**Fig. 6A**). This observation implies that the source of the low-$\delta^{18}O$ signature is located predominantly to the east (trenchward) and towards the boundary with accreted terranes of the Eastern Province. We propose that the low-$\delta^{18}O$ signal and the transitional isotope signature of the CID and EID can be explained in part by partial melting/assimilation of a west-dipping, low-$\delta^{18}O$ terrane that underlies the Median Batholith. The inflection of the isotope gradient near the Grebe-Indecision Creek Shear Zone suggests that the low-$\delta^{18}O$ terrane is a steeply dipping and possibly listric feature consistent with an underthrusted relationship to the Gondwana margin. This suggestion is supported by multichannel seismic images which display a thin, lower-crustal terrane that extends from the Eastern Province and continues below the Median Batholith (Davey, 2005).

Although previous workers have recognized that the Mesozoic Median Batholith has undergone a complex history of polymetamorphism and collisional/transpressional deformation, the precise timing of these events remains unclear particularly in the context of juxtaposition of the Eastern and Western province and the origin of the low-$\delta^{18}O$ source in Fiordland. Models for the juxtaposition of the Eastern and Western provinces generally fall into two tectonic scenarios: 1) Late Jurassic to Early Cretaceous collision involving the Western Province and a fringing-arc Eastern Province terrane such as the outboard Median Batholith (McCulloch et al., 1987; Kimbrough et al., 1994; Muir et al., 1995; Adams et al., 1998; Mortimer et al., 1999a; Scott et al., 2009, 2011; Scott, 2013), and/or 2) Permian collision of the Brook Street Terrane with the

Western Province (Mortimer et al., 1999; McCoy-West et al., 2014). Examination of spatial-isotope data with $^{206}Pb/^{238}U$ zircon ages from Darran Suite samples in the Lake Manapouri area demonstrates that the prominent east-west isotope gradient in the CID/EID was in place by at least 160 Ma (**Fig. 7A-B**). In addition, xenoliths of unknown age in Triassic plutonic rocks in northern Fiordland also record low-$\delta^{18}O$ bulk-rock values below 4‰ and as low as -12.4‰. The low-$\delta^{18}O$ xenoliths are contained within host rocks that have much higher values (typically ~4-7.5‰) suggesting that they were not simply altered along with the surrounding rocks, but instead record the presence of a low-$\delta^{18}O$ source at depth. Collectively, these data indicate that the low-$\delta^{18}O$ source in Fiordland predates the Jurassic (Blattner and Williams, 1991). Thus, we conclude that the development of the spatial-isotope gradient in Fiordland cannot be attributed to Late Jurassic or Early Cretaceous contraction and must have been produced by an earlier event/process. Our data do not permit us to directly determine the timing of amalgamation between the Eastern and Western provinces; however, a Permian amalgamation event as proposed by McCoy-West et al. (2014) is consistent with our data.

The three arc-parallel isotope domains in the Median Batholith are also bounded by major Cretaceous ductile transpressional shear zones, and this observation suggests that they are in some way related to the development and/or modification of the isotope domains in Fiordland (**Figs. 1 and 6**). Previous studies have documented that these shear zones are long-lived lithospheric-scale features that were periodically reactivated during various tectonic events from the Cretaceous to the Miocene (Marcotte et al., 2005; Scott et al., 2009; Buriticá et al., 2019; Klepeis et al., 2019a,b). In particular, the Grebe–Indecision Creek Shear Zone system has been postulated to be a paleo-suture zone between the Eastern and Western provinces (Marcotte et al., 2005; Scott et al., 2009). The following features support this interpretation (see also Scott, 2013):

(1) the Grebe–Indecision Creek Shear Zone system delineates the easternmost distribution of the Takaka Terrane (and thus the Western Province) and marks a strong change in $\delta^{18}O$ and Hf (Zrn) isotope values between the EID and the WID/CID, (**Fig. 1**), (2) Late Cambrian and mid-Paleozoic plutons are primarily located west of the Grebe–Indecision Creek Shear Zone system (Scott et al., 2009), and (3) the Grebe Shear Zone–Indecision Creek Shear Zone system extends along the entire length of the Fiordland region and parallels the Mesozoic paleo-arc axis (Marcotte et al., 2005; Scott et al., 2009).

The Early Cretaceous George Sound Shear Zone delineates the WID-CID boundary and also represents a deep-seated, arc-parallel, crustal-scale boundary. Isotopically, εHf (Zrn) values do not show a significant change across the WID-CID boundary; however, $\delta^{18}O$ (Zrn) values do show a decrease from WID values and we also observe significant $\delta^{18}O$ (Zrn) variability in this zone (**Fig. 5A**). Geologically, the WID-CID boundary also coincides with an elongate string of Carboniferous plutons that form an arc-parallel lineament which predates Early Cretaceous magmatism and the formation of the George Sound Shear Zone (see Heterogenous Paleozoic plutonic complexes: Fig. 1). These plutons signify that the region now defined by the George Sound Shear Zone was a zone of focused magmatism in the Carboniferous (Klepeis et al. 2019b). Moreover, Carboniferous L-tectonites in the area indicate the existence of an older inherited shear zone, which spatially coincides with the Early Cretaceous George Sound Shear Zone (Lindquist, 2020). In Northern Fiordland, Early Cretaceous, lower-crustal plutons extending to ca. 50 km paleodepth are also centered on this structural lineament (Klepeis et al., 2004; Allibone et al., 2009), indicating that magmas leaked up along a deep-crustal structure during the Early Cretaceous flare-up. The same structural feature extends along strike southward and upward in the crust in central Fiordland where it coincides with voluminous mid-crustal plutons of the inboard Separation Point Suite (Blatchford et al., 2020). Finally, this lineament has been reactivated several times in the past: as the George Sound Shear Zone in the Early Cretaceous, and most recently by Miocene thrust faults (Klepeis et al., 2019a,b). Collectively, these features suggest that the WID-CID boundary is a deep-seated and long-lived structural feature which was periodically reactivated for over 300 Myr.

Although our data show that Early Cretaceous transpression was not responsible for the formation of the spatial-isotope gradient in Fiordland, it did have an effect on the present-day spatial isotope pattern. Because transpression involves simultaneous horizontal shortening, lateral translation and, possibly, vertical extrusion, the net result is an apparent steepening of the isotope gradient and greater isotope variability in regions affected by transpression (Harland, 1971; Sanderson and Marchini, 1984; Fossen et al., 1994; Dewey et al., 1998). The effects of transpression are observed primarily at the boundary between the CID and EID, and to a lesser extent at the WID-CID boundary, where shortening and vertical extrusion functioned to shorten the isotope gradient and produce a deflection of the isotope trend where transpression/extrusion was localized (**Fig. 5**). A classic example of similar shortening of isotope ratios is observed in the Western Idaho Shear Zone, where the $^{87}Sr/^{86}Sr$ isotope gradient across the Idaho batholith was steepened by syn-magmatic transpressional movement (Giorgis et al., 2005).

The geologic relationships we observe in the Median Batholith are shown in a block model in **Figure 8** which illustrates present-day relationships between plutons, shear zones and their spatial-isotope geochemistry. The diagram highlights the three isotope domains that are bounded by lithospheric-scale structural features, namely the George Sound Shear Zone and the Grebe-Indecision Creek Shear Zone system. As described above, our data support the assertion presented in Marcotte et al. (2005) and Scott (2013) that the Grebe-Indecision Creek Shear Zone system represents a fundamental lithospheric-scale fault zone that separates the Eastern and Western provinces and accreted terranes of the Eastern Province from the ancient Gondwana margin. In our interpretation, Median Batholith plutons in the EID intruded Eastern Province crust which is only exposed at the surface as isolated metasedimentary rocks (Scott, 2013). Thus, we postulate that the EID is underlain by a previously unrecognized, mafic low-$\delta^{18}O$ terrane which now extends beneath the EID and CID and thins to the west (continentward).

Temporal Isotope Trends in Mesozoic Magmatism

The spatial isotope zonation that we observe forms the backdrop for understanding temporal variation in arc magmatism and continental crust production in the Median Batholith. Zircon age data confirm earlier observations by Tulloch and Kimbrough (2003) that Mesozoic arc construction involved two distinct magmatic trends which include: i) a prolonged, >100 Myr period of Late Triassic to Early Cretaceous, low-Sr/Y, Darran Suite magmatism which was spatially focused within a ~20 km-wide zone centered on and west of the Grebe Shear Zone–Indecision Creek Shear Zone in Fiordland (blue band in **Fig. 9**), and ii) a brief flare-up event, ~20 Myr in duration, consisting of high-Sr/Y magmatism (Separation Point Suite, including Western Fiordland Orthogneiss) that occurred in association with abrupt widening and continentward migration of the Early Cretaceous arc axis (green band in **Fig. 9**). The focusing of Darran Suite magmatism in the Grebe Shear Zone–Indecision Creek Shear Zone and the CID/EID boundary for >100 Myr further substantiates the notion that this zone is a major lithospheric zone of weakness that formed prior to Mesozoic magmatic activity. Moreover, the location of Darran Suite magmatism at the CID/EID boundary is also not random, but instead reflects magmatic exploitation of a deep-seated, lithospheric scale fault system. This focusing of magmatism along an arc-parallel, lithospheric scale shear zone is also observed along the George Sound Shear Zone in Fiordland and in other Cordilleran arc systems such as the Western Idaho Shear Zone (Giorgis et al., 2005) and the southern Sierra Nevada Batholith (e.g., Saleeby et al., 2008).

In contrast to the largely static nature of the Darran Suite, the Separation Point Suite (including the Western Fiordland Orthogneiss) is characterized by sweeping migration of high-Sr/Y magmas across all three isotope domains from 129-110 Ma (**Fig. 9**). Buriticá et al. (2019) noted that during this time, the width of the Mesozoic arc reached at least 70 km in Fiordland which is twice the average width of modern arcs (Ducea et al., 2015b; 2017). This is a minimum value since the western margin of the Median Batholith is truncated by the Alpine Fault, and Cretaceous and Miocene contraction has shortened the region after magmatic emplacement. This transition from largely spatially fixed magmatism at the EID/CID boundary for >100 Myr to abrupt continentward arc migration across the EID to the WID signifies an important change in arc dynamics, which we explore later.

Figure 10 shows temporal isotope variations in the Median Batholith and illustrates several important isotope trends in our data. Temporal variations in O-isotopes show that the migration of the arc axis through time resulted in variable crustal recycling of the low-$\delta^{18}O$ source, and this recycling decreased dramatically during Separation Point Suite magmatism (**Fig. 10A**). During the Early Cretaceous flare-up, zircon O-isotope data overlap the high-temperature mantle field as measured by SIMS (Valley, 2003) and we see no evidence to support significant involvement of high-$\delta^{18}O$ sources like those that characterize supracrustal rocks in the region (see Decker et al., 2017 and modeling results below).

In the CID and EID, some zircons lie well below the high-temperature mantle field, and such low-$\delta^{18}O$ zircons are rare in arc-related environments. Most zircons formed in arcs typically have $\delta^{18}O$ values between 5 and 10‰ consistent with mantle influences and/or interaction with rocks altered under low-temperature conditions (~250°C) (Valley, 2003; Cavosie et al., 2011). In contrast, low-$\delta^{18}O$ zircons (<5‰) are typically restricted to extensional or rift-related environments where rock-water interactions occur at temperatures exceeding 300°C (Bindeman and Valley, 2001; Zheng et al., 2004; Blum et al., 2016). In our study, low-$\delta^{18}O$ zircons also occur over a broad region and their distribution parallels both the Mesozoic arc axis and the paleo-Pacific Gondwana margin (**Fig. 6**). Unlike low-$\delta^{18}O$ zircons formed in rift-related environments, Median Batholith zircons formed in a continental arc setting where the arc axis was either stable for long-periods of time (Darran Suite) or was advancing continentward (Separation Point Suite). We hypothesize that low-$\delta^{18}O$ zircons in the Median Batholith formed by partial melting and recycling of a deeply buried, hydrothermally altered, low-$\delta^{18}O$ terrane which predominately underlies the EID and decreases in abundance westward beneath the CID. The origin of this putative underthrust terrane remains unknown and requires additional study.

Zircon Hf-isotope data provide further evidence into the nature of the crust beneath the Median Batholith and illustrate temporal changes in magma chemistry through time (**Fig. 10B**). Our data show that Darran Suite zircons have strongly positive initial ε_{Hf} (Zrn) values (>+7), though these values are significantly less radiogenic than expected for direct partial melting of Cretaceous depleted mantle (~+15: Vervoort and Blichert-Toft, 1999) or average modern island-arcs (~+13: Dhuime et al., 2011). Initial ε_{Hf} (Zrn) values significantly decreased during Separation Point Suite magmatism, similar to observations of Milan et al. (2017). Our data also show that zircon O and Hf isotopes are decoupled for Separation Point Suite rocks, whereby low positive εHf values correspond to mantle-like-$\delta^{18}O$ values. This observation makes the Separation Point Suite flare-up distinct from those observed in other low-latitude Cordilleran arcs which are characterized by much higher $\delta^{18}O$ (Zrn) values and unradiogenic Hf isotope values (**Fig. 8A-C**) (Chapman et al., 2017).

To investigate magma sources and quantify the amount of crustal recycling in the Median Batholith, we conducted a series of assimilation fractional crystallization (AFC) models (**Fig. 11**). In modeling lower crustal rocks in the Western Fiordland Orthogneiss (**Fig. 11A**), we use average Cretaceous Pacific-Antarctic MORB compositions (Park et al., 2019), Eastern Province sedimentary rocks (Blattner and Reid, 1982; Adams et al., 2005), and Paleozoic I-type rocks (Turnbull et al., 2020). For Eastern Province sedimentary rocks, ε_{Hf} values were calculated from average ε_{Nd} values using the Vervoort et al. (1999) crustal Hf-Nd relationship. For plutonic rocks in the CID and EID, we use the range of WFO melt compositions from **Figure 11A**, and for the low-$\delta^{18}O$ source we use average $\delta^{18}O$ bulk-rock values uncorrected for SiO_2 from 29 samples of the Largs Terrane and related xenoliths in Northern Fiordland reported in Blattner and Williams (1991). The values we use for the low-$\delta^{18}O$ source are $\delta^{18}O(WR) = -1.2‰$, εHf = 10, and Hf concentration = 6 ppm. The average value of the low-$\delta^{18}O$ source is quite low globally compared to other arc terranes, but these values are supported by the presence of low-$\delta^{18}O$ values in Largs Terrane which extend to -12.4. Low-$\delta^{18}O$ values also occur in the Western Fiordland Orthogneiss where Decker (2016) reported xenocrystic Paleozoic $\delta^{18}O$ zircon values as low as -7.0‰. Thus, low-$\delta^{18}O$ rocks extend beyond the footprint of the Largs Terrane in Northern Fiordland and document that very low-$\delta^{18}O$ values are present in the region.

For the WID, lower crustal zircons plot along the mantle array, and relative to Cretaceous Pacific-Antarctic MORB, they have lower εHf values than expected for direct partial melting of a depleted mantle wedge (**Fig. 11A**). To explain these features, we consider two scenarios: assimilation and fractional crystallization of an amphibolitic, Paleozoic I-type arc root (McCulloch et al., 1987) and assimilation of Eastern Province sediments via melting of recycled trench sediments (**Fig. 11A**). For the first scenario, McCulloch et al. (1987) and Tulloch and Kimbrough (2003) proposed that WFO melts formed from partial melting of a mid- to late Paleozoic crustal protolith by underplating of basaltic melts. Paleozoic I-type rocks form part of the pre-batholithic architecture of Fiordland, and we model potential AFC processes in **Figure 11A** using known compositions in the region (see yellow curve: Turnbull et al., 2016; Turnbull et al., 2020). Results of our AFC calculations indicate that WFO melts can be described by 10 to 100% assimilation of Paleozoic I-type host rocks (average assimilant = ~40%). Direct partial melting of Paleozoic I-type rocks can also reproduce the WFO data, but WFO $\delta^{18}O$ (Zrn) values lower than the Paleozoic I-type rocks are difficult to attribute to remelting (or AFC) processes. While significant remelting and/or assimilation of Paleozoic I-type rocks does reproduce the WFO data, these models require extraordinarily high heat flow to induce widespread lower crustal melting. Field studies in the lower crust of Fiordland document little evidence for widespread intracrustal partial melting (Allibone et al., 2009b; Schwartz et al., 2016), and this observation is supported by a number of studies that have challenged the efficiency of intracrustal melting of amphibolites as a mechanism for voluminous melt production in the lower crust (Bergantz, 1992; Petford & Gallagher, 2001; Dufek & Bergantz, 2005; Annen et al., 2006; Solano et al., 2012; Walker et al., 2015). Given the outcrop area of the Separation Point Suite (8200 km^2) and an ~19 Myr duration of flare-up magmatism (129-110 Ma), we calculate an areal addition rate of ~600 km^2/Myr and a magma addition rate of 11,700 km^3/Myr assuming a 20 km plutonic root for the WFO (Klepeis et al., 2007; 2019b). These calculated rates are similar to those for some of the largest flare-ups worldwide (Paterson and Ducea, 2015) and requires very high magma production rates.

Collins et al. (2020) proposed an alternative mechanism for the generation of intermediate to felsic melts in Cordilleran arcs that side-steps thermodynamic issues of earlier models associated with melting of amphibolite by underplating. In their model, tonalitic to trondhjemitic melts are generated by fluid-fluxed partial melting of the lower crust, which is driven by the addition of external aqueous fluids derived from the crystallization of mantle-derived hydrous melts. In their model, they show that the addition of ~4.5 wt. % H_2O to a dioritic underplate results in ~30-40% melt production at temperatures of 750 to 900° C. Fluid-fluxed partial melting of the lower crust thus produces wet, low-temperature (<800 °C), intermediate to felsic melts like those observed in Cordilleran batholiths worldwide (Collins et al, 2020). As with direct partial melting described above, fluid-fluxed partial melting of Paleozoic I-type rocks would reproduce some of the WFO zircons; however, ~20% of the WFO zircons have $\delta^{18}O$ values below the reported range of Paleozoic I-type rocks. The effect of introducing external aqueous fluids on melt composition is dependent on fluid composition and temperature of rock-fluid interaction. At high temperatures, fluid-rock interaction could have the effect of driving $\delta^{18}O$ melt towards lower values, and if the only source is the Paleozoic I-type rocks, this process could reproduce the WFO zircon data. Contributions from associated high-$\delta^{18}O$ metasedimentary rocks in the lower crust (e.g., Deep Cove Gneiss) would have the opposite effect and would drive $\delta^{18}O$ melt values towards higher values compared to the Paleozoic I-type rocks. Thus, fluid-fluxed partial melting of Paleozoic I-type rocks is permissible provided that high-$\delta^{18}O$ metasedimentary rocks were not significantly involved.

Fluid-fluxed partial melting is also expected to produce low-temperature (<800 °C), intermediate to felsic melts; however, in the lower crust of Fiordland, WFO crystallization temperatures are higher than expected for hydrous melts predicted by the Collins et al. model (see path 'C' in their Fig. 2). In the case of the WFO, igneous amphibole crystallization temperatures range from 960 to 810 °C (Carty et al., 2019 in review) and igneous zircon give temperatures ranging from 950 to 750 °C for (Schwartz et al., 2017; Bhattacharya et al., 2018). These temperatures generally match those for fractionated andesites and dacites in the Deep Crustal Hot Zone model of Annen et al. (2006) (see path 'B' in Fig. 2 of Collins et al., 2020). They also agree with temperatures observed in crystallization experiments for the generation granodioritic compositions by fractional crystallization processes (Blatter et al., 2013; Nandedkhar et al., 2014; Ulmer et al. 2018). Thus, while $\delta^{18}O$ zircon data is equivocal, igneous thermometry appears to be most consistent with WFO generation by fractional crystallization from a high-temperature, mafic to intermediate melt.

Another possibility is that the range in zircon $\delta^{18}O$ and ε_{Hf} in the WFO reflects recycling of trench sediment into arc magmas (e.g., Plank and Langmuir, 1993; Plank, 2005). We model this process using an average depleted mantle melt (Antarctic-Pacific MORB) and an Eastern Province sediment (Torlesse sediment). Modeling results are shown by two dashed blue curves in **Fig. 11A** which demonstrate that WFO zircons are well described by ~10-20% assimilation of subducted supracrustal material. Modeling of Sr-Nd-Pb isotope data from the WFO yield similar results (Carty et al. in review), and these results are also consistent with the those of Decker et al. (2017) who modeled various sedimentary sources and concluded that WFO melts included up to 15% recycled sediment. We conclude that incorporation of low degrees of trench sediment into arc melts beneath the Median Batholith can explain the stable and radiogenic isotope characteristics of the WFO. Other processes (e.g., fluid-fluxed melting) may also have operated as secondary processes particularly in the generation of felsic dikes (Bhattacharya et al., 2018).

Compared to the WFO, EID and CID zircons are displaced to lower $\delta^{18}O$ values reflecting interaction with a low-$\delta^{18}O$ source (c.f., CID and EID zircons versus red 'WFO' field in **Fig. 11B-C**). Results from AFC models demonstrate that CID and EID zircons can be described by 0-20% and 10-30% and assimilation, respectively, of a low-$\delta^{18}O$ source by a lower-crustal melt as observed in the WID. Therefore, we propose that EID and CID zircons formed from crystallization of hybrid melts produced by mixing/assimilation of WFO-like melts with low-$\delta^{18}O$, hydrothermally altered mafic crust. This hybridization may have occurred in the lower crust in a MASH or hot zone (Hildreth and Moorbath, 1988; Annen et al., 2006) and/or during ascent through the crust in central and eastern Fiordland. Assimilation and/or mixing of hydrothermally altered mafic crust is consistent with bulk-rock chemistry of the Separation Point Suite rocks in the EID which have high-average bulk-rock SiO_2 values (>70 wt.%), and trend toward peraluminous values. Separation Point Suite granitic rocks in the EID are also characterized by high-Sr/Y values (>90) and depletions in heavy rare earth elements, features which are consistent with involvement of garnet as a residual or fractionating phase in the lower crust (Muir et al., 1995). Direct partial melting of a less extreme, low-$\delta^{18}O$ source (~3-4‰) is also possible, though strongly negative $\delta^{18}O$ whole-rock values (down to -12‰) are documented in Northern Fiordland (Blattner and Williams, 1991; Decker, 2016).

The modeling results shown in **Figure 11** imply two important features: 1) the low-$\delta^{18}O$ source is strongest in the EID, diminishes in the CID, and is absent in the WID, and 2) a common 'WFO-like' source (red zircons and red fields in **Fig. 11**) is present in all isotope domains and magmatic suites in the Mesozoic Median Batholith (i.e., both Darran and Separation Point suites) irrespective of age or trace-element chemistry. This 'WFO-like' source is characterized by mantle-like δ^{18}O (Zrn) values and εHf values of ~+1 to +5 and is progressively contaminated in the CID and EID by a low-δ^{18}O source. The observation of a 'WFO-like' signal in both Darran and Separation Point suites indicates the presence of a stable, and long-lived (>100 Myr), source component/process which we interpret as reflecting recycling of Eastern Province sediments in arc magmas beneath the Median Batholith. Below we explore implications for stable isotope domains and transient processes in the Median Batholith.

Temporally Stable versus Transient Petrogenetic Processes

In a global study of spatial isotope trends in Cordilleran arcs, Chapman et al. (2017) noted that some arcs are characterized by a temporal persistence of consistent radiogenic isotope signatures in a given geographic region. They suggested that this temporal persistence indicates a stable petrogenetic mechanism such as long-term contamination of the melt region and/or assimilation in a lower-crustal 'MASH' or Deep Crustal Hot Zone (Hildreth and Moorbath, 1988; Annen et al., 2006). In other cases where isotope signatures change through time in the same geographic region, they suggested that temporally transient processes may have been active such as relamination, forearc erosion, slab tears, and continental underthrusting. They note that temporally transient processes are distinguished by discrete excursions in temporal isotope trends resulting in melts of contrasting isotope compositions within the same geographic region (Chapman et al., 2017).

In the Median Batholith, we observe a combination of both stable and transient temporal isotope trends (**Fig. 10A-B**). Stable temporal isotope trends are best illustrated by δ^{18}O (Zrn) in the EID and in the CID. In these geographically controlled isotope domains, we observe that from ca. 170 to 120 Ma, $\delta^{18}O$ (Zrn) values remained nearly unchanged for 40-50 Myr despite geochemical transitions from low-Sr/Y (Darran Suite) to high-Sr/Y (Separation Point Suite) (see 'EID and CID Isotope trend' lines in **Fig. 10A**). The consistency of $\delta^{18}O$ (Zrn) values in the EID and CID through time can be explained by a stable petrogenetic mechanism like the one we model in **Figure 11B-C** whereby 'WFO-like' melts assimilated mafic, low-$\delta^{18}O$ crust in relatively fixed proportions over at least 50 Myr. We note that this stable petrogeneic process involves two stages: 1) production of 'WFO-like' melts by recycling of trench sediments, and 2) remelting/assimilation of low-$\delta^{18}O$ crust either during ascent or in a lower-crustal MASH/hot zone. Superimposed on this long-lived and stable petrogenetic process is the temporal transition from low-Sr/Y to high-Sr/Y values observed in both the EID and CID. The latter change in trace-element chemistry is consistent with crustal thickening of the arc in this location at or before 129 Ma and signifies the production of a garnet-bearing root (Muir et al., 1995).

Radiogenic isotope data show more complexity and evidence for both temporally stable and punctuated petrogenetic processes. Evidence for temporally stable petrogenetic processes is again observed in the EID where initial ε_{Hf} (Zrn) also remained consistently positive (ε_{Hf} =+7 to +8) for ~40 Myr (see 'EID isotope trend' in **Fig. 10B**). In contrast, the CID displays evidence for temporal changes in isotope composition with initial ε_{Hf} (Zrn) decreasing from +8 at ca. 165 Ma to +6 to +3 Ma at ca. 129-110 Ma. These features are also observed in a compilation of bulk-rock Sr- and Nd- isotope data (Milan et al., 2017). While ε_{Hf} (Zrn) values decrease through time, $\delta^{18}O$ (Zrn) values increase from low-$\delta^{18}O$ values to 'mantle-like' values during the terminal arc-magmatic flare-up in Early Cretaceous (**Fig. 10)**. Thus, the 'mantle-like' source became increasingly volumetrically significant during the terminal Separation Point Suite flare-up starting at ca 129 Ma (see inflection in blue and red trends in **Figs. 10A and B**), and the presence of this strong mantle-like $\delta^{18}O$ (Zrn) signal distinguishes the Median Batholith from other Cordilleran batholiths which typically show an increase in continental crustal recycling during continentward arc migration (Chapman et al., 2017). These features support a temporally transient process in the Early Cretaceous such as the propagation of a slab tear or slab window (Decker et al. 2017; Schwartz et al. 2017). In addition, the mantle signal is also associated with the widening of the arc axis to >70 km and the abrupt change from a geographically stable magmatic arc axis in the Jurassic to rapid continentward migration in the Early Cretaceous (**Fig. 9**). Previous workers have also noted that after the Early Cretaceous arc flare-up, the arc experienced rapid post-emplacement uplift, extensional orogenic collapse, and widespread A-type magmatism throughout Zealandia Cordillera (Tulloch and Kimbrough, 2003; Kula et al. 2007; Tulloch et al., 2009b; Klepeis et al., 2016; Schwartz et al., 2016). Collectively, these features document a dynamic change in arc processes that are best explained by a temporally transient process that culminated in a cessation of arc magmatic activity.

Implications

Coupled zircon oxygen and hafnium isotope analyses provide a powerful tool to understand the crustal architecture of Cordilleran batholiths and to evaluate spatial and temporal arc magmatic trends. Our zircon Hf and O data show that the isotope architecture of the Median Batholith is partitioned into three isotope domains that reflect deep-seated and spatially controlled source regions that do not directly correlate with the surficial geology. Superimposed on these isotope domains, we confirm that Mesozoic magmatism involved two distinct spatio-temporal trends including: a) a prolonged, >100 Myr period of Late Triassic to Early Cretaceous (Darren Suite), low-Sr/Y magmatism spatially focused within a ~20 km-wide zone centered on and west of the Grebe Shear Zone–Indecision Creek Shear Zone, and b) a brief, ca. 20 Myr long flare-up event, consisting of high-Sr/Y magmatism (Separation Point Suite) that occurred in association with abrupt widening and continentward migration of the Early Cretaceous arc axis. Trends in stable and radiogenic zircon isotope values show evidence for both temporally stable and transient petrogenetic processes that led to the production of Mesozoic continental crust in the Median Batholith. Isotope modeling shows that arc magmatism involved significant production of new continental crust with 0-30% recycling of a low-δ^{18}O source throughout the Median Batholith. The terminal Early Cretaceous arc flare-up primarily involved partial melting of a depleted mantle source contaminated with a recycled trench sediment component (10-20%). Isotope modeling shows that this signal was present in all Mesozoic magmas and reflects a long-lived petrogenetic process. The Separation Point Suite flare-up from 129-110 Ma signified the end of arc magmatism and Mesozoic continental crust production in the Median Batholith.

Acknowledgements

We thank Peter Kuiper of Cruise Te Anau for assistance with rock sampling in Lake Te Anau and Lake Manapouri. The New Zealand Department of Conservation, Te Anau office is also thanked for allowing access and sampling in Fiordland. Jade Star Lackey and Jonathan Harris are thanked for assistance with XRF analyses. We thank Bill Collins and Chris Spencer for insightful and helpful reviews. Financial support for this project was provided by the National Science Foundation grant EAR-1352021 (Schwartz), and NSF-EAR 1649254 (Arizona LaserChron Center). WiscSIMS is supported by NSF (EAR-1658823) and the University of Wisconsin-Madison. CSU Northridge Associated Students, CSU Northridge Graduate Office, and Arizona LaserChron scholarships assisted with travel and research expenses.

References Cited List

Adams, C.J., Pankhurst, R.J., Maas, R., Millar, I.L. (2005) Nd and Sr isotopic signatures of metasedimentary rocks around the South Pacific margin and implications for their provenance. Geological Society of London, Special Publications 246, 113-141.

Adams, C.J., Barley, M.E., Fletcher, I.R., and Pickard, A.L. (1998) Evidence from U-Pb zircon and $^{40}Ar/^{39}Ar$ muscovite detrital mineral ages in metasandstones for movement of the Torlesse suspect terrane around the eastern margin of Gondwanaland. Terra Nova, 10, 183–189.

Allibone, A.H., Jongens, R., Scott, J.M., Tulloch, A.J., Turnbull, I.M., Cooper, A.F., Powell, N.G., Ladley, E.B., King, R.P., and Rattenbury, M.S. (2009a) Plutonic rocks of the Median Batholith in eastern and central Fiordland, New Zealand: Field relations, geochemistry, correlation, and nomenclature. New Zealand Journal of Geology and Geophysics Vol. 52, 101–148.

Allibone, A.H., Jongens, R., Turnbull, I.M., Milan, L.A., Daczko, N.R., De Paoli, M.C., and Tulloch, A.J. (2009b) Plutonic rocks of western Fiordland, New Zealand: Field relations, geochemistry, correlation, and nomenclature. New Zealand Journal of Geology and Geophysics, 52, 379–415.

Annen, C., Blundy, J.D., and Sparks, R.S.J. (2006) The genesis of intermediate and silicic magmas in deep crustal hot zones. Journal of Petrology, 47, 505–539.

Armstrong, R.L. (1988) Mesozoic and early Cenozoic magmatic evolution of the Canadian Cordillera. Geological Society of America Special Papers, 218, 55–91.

Bergantz, G. W. (1992) Conjugate solidification and melting in multicomponent open and closed systems. International Journal of Heat and Mass Transfer, 35, 533–543.

Bindeman, I.N. (2008) Oxygen isotopes in mantle and crustal magmas as revealed by single crystal analysis. Reviews in Mineralogy and Geochemistry, 69, 445–478.

Bindeman, I.N., and Valley, J.W. (2001) Low-δ^{18}O Rhyolites from Yellowstone: Magmatic evolution based on analyses of zircons and individual phenocrysts. Journal of Petrology, 42, 1491–1517.

Bishop, D.G., Bradshaw, J.D., Landis, C.A. (1985) Provisional terrane map of South Island, New Zealand. In D.G. Howell, Ed., Tectonostratigraphic Terranes of the Circum-Pacific Region, AAPG Circum-Pacific Council for Energy and Mineral Resources Earth Science Series, 1, 515-521.

Blatchford, H.J., Klepeis, K.A., Schwartz, J.J., Jongens, R., Turnbull, R.E., Miranda, E.A., Coble, M.A., Kylander-Clark, A.R.C. (2020) Interplay of Cretaceous transpressional deformation and continental arc magmatism in a long-lived crustal boundary, central Fiordland. Geosphere, 16, https://doi.org/10.1130/GES02251.1

Blatter, D. L., Sisson, T. W. & Hankins, W. B. (2017) Voluminous arc dacites as amphibole reaction-boundary liquids. Contributions to Mineralogy and Petrology, 172, 1-37.\

Blattner, P., & Reid, F. (1982) The origin of lavas and ignimbrites of the Taupo Volcanic Zone, New Zealand, in the light of oxygen isotope data. Geochimica et Cosmochimica Acta, 46(8), 1417–1429. doi:10.1016/0016-7037(82)90276-9

Blattner, P., and Williams, J.G. (1991) The Largs high-latitude oxygen isotope anomaly (New Zealand) and climatic controls of oxygen isotopes in magma. Earth and Planetary Science Letters, 103, 270–284.

Blum TB, Kitajima K, Nakashima D, Strickland A, Spicuzza MJ, Valley JW (2016) Oxygen isotope evolution of the Lake Owyhee volcanic field, Oregon, and implications for low-

δ^{18}O magmatism of the Snake River Plain - Yellowstone hotspot and other low-δ^{18}O large igneous provinces, Contributions to Mineralogy and Petrology, 171, 23p.

Bolhar, R., Weaver, S.D., Whitehouse, M.J., Palin, J.M., Woodhead, J.D., and Cole, J.W. (2008) Sources and evolution of arc magmas inferred from coupled O and Hf isotope systematics of plutonic zircons from the Cretaceous Separation Point Suite (New Zealand). Earth and Planetary Science Letters, 268, 312–324.

Bradshaw, J.D. (1993) A review of the Median Tectonic Zone: terrane boundaries and terrane amalgamation near the Median Tectonic Line. New Zealand Journal of Geology and Geophysics, 36, 117–125.

Buriticá, L.F., Schwartz, J.J., Klepeis, K.A., Miranda, E.A., Tulloch, A.J., Coble, M.A., and Kylander-Clark, A.R.C. (2019) Temporal and spatial variations in magmatism and transpression in a Cretaceous arc, Median Batholith, Fiordland, New Zealand. Lithosphere, 11, 652–682.

Campbell, M.J., Rosenbaum, G., Allen, C.M., and Mortimer, N. (2020) Origin of dispersed Permian–Triassic fore-arc basin terranes in New Zealand: Insights from zircon petrochronology. Gondwana Research, 78, 210-227.

Cavosie, A.J., Valley, J.W., Kita, N.T., Spicuzza, M.J., Ushikubo, T., and Wilde, S.A. (2011) The origin of high δ^{18}O zircons: marbles, megacrysts, and metamorphism. Contributions to Mineralogy and Petrology, 162, 961–974.

Cecil, M.R., Gehrels, G., Ducea, M.N., and Patchett, P.J. (2011) U-Pb-Hf characterization of the central Coast Mountains batholith: Implications for petrogenesis and crustal architecture. Lithosphere, 3, 247–260.

Chapman, A.D., Saleeby, J.B., and Eiler, J. (2013) Slab flattening trigger for isotope disturbance and magmatic flareup in the southernmost Sierra Nevada batholith, California. Geology, 41, 1007–1010.

Chapman, J.B., Ducea, M.N., Kapp, P., Gehrels, G.E., and DeCelles, P.G. (2017) Spatial and temporal radiogenic isotope trends of magmatism in Cordilleran orogens. Gondwana Research, 48, 189–204.

Chapman, J.B., Dafov, M.N., Gehrels, G., Ducea, M.N., Valley, J.W., Ishida, A. (2018) Lithospheric architecture and tectonic evolution of the southwestern U.S. Cordillera: constraints from zircon Hf and O isotope data. Geological Society of America Bulletin, 130, 2031-2046.

Collins, W.J., Murphy, B.J., Johnson, T.E., and Huang, H-Q. (2020) Critical role of water in the formation of continental crust. Nature Geoscience, 13, 331-338.

Coombs, D.S., Landis, C.A., Norris, R.J., Sinton, J.M., Borns, D.J., Craw, D. (1976) The Dun Mountain Ophiolite Belt, New Zealand, its tectonic setting, constitution and origin, with special reference to the southern portion. American Journal of Science, 276, p. 561-603

Coombs, D.S. (1985) New Zealand terranes. Third Circum-Pacific Terrane Conference: Geological Society of Australia abstracts, 14, 45–48.

Cooper, R.A., and Tulloch, A.J. (1992) Early Palaeozoic terranes in New Zealand and their relationship to the Lachlan Fold Belt. Tectonophysics, 214, 129–144.

Davey, F.J. (2005) A Mesozoic crustal suture on the Gondwana margin in the New Zealand region. Tectonics, 24, 1–17.

de Silva, S.L., Riggs, N.R., and Barth, A.P. (2015) Quickening the pulse: Fractal tempos in continental arc magmatism. Elements, 11, 113–118.

DeCelles, P.G., and Graham, S.A. (2015) Cyclical processes in the North American Cordilleran orogenic system. Geology, 43, 499–502.

DeCelles, P.G., Ducea, M.N., Kapp, P., and Zandt, G. (2009) Cyclicity in Cordilleran orogenic systems. Nature Geoscience, 2, 251–257.

Decker, M. (2016). Triggering mechanisms for a magmatic flare-up of the lower crust in Fiordland, New Zealand, from U–Pb zircon geochronology and O–Hf zircon geochemistry. MS thesis, California State University Northridge, 122 pp.

Decker, M.F.I., Schwartz, J.J., Stowell, H.H., Klepeis, K.A., Tulloch, A.J., Kitajima, K., Valley, J.W., and Kylander-Clark, A.R.C. (2017) Slab-Triggered Arc Flare-up in the Cretaceous Median Batholith and the Growth of Lower Arc Crust, Fiordland, New Zealand. Journal of Petrology, 58, 1145–1171.

Dewey, J.F., Holdsworth, R.E., and Strachan, R.A. (1998) Transpression and transtension zones. Geological Society Special Publication, 135, 1–14.

Dhuime, B., Hawkesworth, C.J., and Cawood, P. (2011) When continents formed. Science, 331, 154–155.

Dickinson, W.R. (1997) Overview: Tectonic implications of Cenozoic volcanism in coastal California. Geological Society of America Bulletin, 109, 936–954.

Ducea, M.N. (2002) Constraints on the bulk composition and root foundering rates of continental arcs: A California arc perspective. Journal of Geophysical Research: Solid Earth, 107, ECV 15-1-ECV 15-13.

Ducea, M.N., and Barton, M.D. (2007) Igniting flare-up events in Cordilleran arcs. Geology, 35, 1047–1050.

Ducea, M.N., Seclaman, A.C., Murray, K.E., Jianu, D., and Schoenbohm, L.M. (2013) Mantle-drip magmatism beneath the Altiplano-Puna plateau, central Andes. Geology, 41, 915–918.

Ducea, M.N., Saleeby, J.B., and Bergantz, G.W. (2015a) The Architecture, Chemistry, and Evolution of Continental Magmatic Arcs. Annual Review of Earth and Planetary Sciences, 43, 299–331.

Ducea, M.N., Paterson, S.R., and DeCelles, P.G. (2015b) High-volume magmatic events in subduction systems. Elements, 11, 99–104.

Ducea, M.N., Bergantz, G.W., Crowley, J.L., and Otamendi, J. (2017) Ultrafast magmatic buildup and diversification to produce continental crust during subduction. Geology, 45, 235–238.

Dufek, J. & Bergantz, G. W. (2005) Lower crustal magma genesis and preservation: A stochastic framework for the evaluation of basalt-crust interaction. Journal of Petrology, 46, 2167–2195.

Fisher, C.M., Vervoort, J.D., and Dufrane, S.A. (2014) Accurate Hf isotope determinations of complex zircons using the “laser ablation split stream” method. Geochemistry, Geophysics, Geosystems, 15, 121–139.

Fossen, H., Tikoff, B., and Teyssier, C. (1994) Strain modeling of transpressional and transtensional deformation. Norsk Geologisk Tidsskrift, 74, 134–145.

Frost, C.D., and Coombs, D.S. (1989) Nd isotope character of New Zealand sediments: implications for terrane concepts and crustal evolution. American Journal of Science. vol and p ?

DOI: https://doi.org/10.2138/am-2021-7626. http://www.minsocam.org/

Gibson, G.M., and Ireland, T.R. (1996) Extension of Delamerian (Ross) orogen into western New Zealand: Evidence from zircon ages and implications for crustal growth along the Pacific margin of Gondwana. Geology, 24, 1087–1090.

Giorgis, S., Tikoff, B., and McClelland, W. (2005) Missing Idaho arc: Transpressional modification of the $^{87}Sr/^{86}Sr$ transition on the western edge of the Idaho batholith. Geology, 33, 469–472.

Hacker, B.R., Kelemen, P.B., and Behn, M.D. (2011) Differentiation of the continental crust by relamination. Earth and Planetary Science Letters, 307, 501–516.

Harland, W.B. (1971) Tectonic transpression in Caledonian Spitsbergen. Geological Magazine, 108, 27–41.

Hawkesworth, C.J., Dhuime, B., Pietranik, A.B., Cawood, P.A., Kemp, A.I.S., and Storey, C.D. (2010) The generation and evolution of the continental crust. Journal of the Geological Society, 167, 229–248.

Hildreth, W., and Moorbath, S. (1988) Crustal contributions to arc magmatism in the Andes of Central Chile. Contributions to Mineralogy and Petrology, 98, 455–489.

Jongens, R. (1997) The Anatoki Fault and Structure of the Adjacent Buller and Takaka Terrane Rocks, Northwest Nelson, New Zealand, 424 p. Ph.D. thesis, University of Canterbury.

Jongens, R. (2006) Structure of the Buller and Takaka Terrane rocks adjacent to the Anatoki Fault, northwest Nelson, New Zealand. New Zealand Journal of Geology and Geophysics, 49, 443–461.

Kay, S.M., Coira, B., and Viramonte, J. (1994) Young mafic back arc volcanic rocks as indicators of continental lithospheric delamination beneath the Argentine Puna Plateau, Central Andes. Journal of Geophysical Research, 99, 24323–24339.

Kay, S.M., Godoy, E., and Kurtz, A. (2005) Episodic arc migration, crustal thickening, subduction erosion, and magmatism in the south-central Andes. Geological Society of America Bulletin, 117, 67–88.

Kemp, A.IS.., Hawkesworth, C.J., Foster, G.L., Paterson, B.A., Woodhead, J.D., Hergt, J.M., Gray, C.M., & Whitehouse, M.J. (2007) Magmatic and crustal differentiation history of granitic rocks from Hf-O isotopes in zircon. Science, 315, 980–983

Kimbrough, D.L., Tulloch, A.J., Coombs, D.S., Landis, C.A., Johnston, M.R., and Mattinson, J.M. (1994) Uranium-lead zircon ages from the Median Tectonic Zone, New Zealand. New Zealand Journal of Geology and Geophysics, 37, 393–419.

Kita, N.T., Ushikubo, T., Fu, B., and Valley, J.W. (2009) High precision SIMS oxygen isotope analysis and the effect of sample topography. Chemical Geology, 264, 43–57.

Klepeis, K.A., Schwartz, J.J., Stowell, H.H., and Tulloch, A.J. (2016) Gneiss domes, vertical and horizontal mass transfer, and the initiation of extension in the hot lower-crustal root of a continental arc, Fiordland, New Zealand. Lithosphere, 8, 116–140.

Klepeis, K.A., Webb, L.E., Blatchford, H.J., Jongens, R., Turnbull, R.E., and Schwartz, J.J. (2019a) The Age and Origin of Miocene-Pliocene Fault Reactivations in the Upper Plate of an Incipient Subduction Zone, Puysegur Margin, New Zealand, Tectonics Vol. 38, 3237–3260.

Klepeis, K., Webb, L., Blatchford, H., Schwartz, J., Jongens, R., Turnbull, R., and Stowell, H. (2019b) Deep slab collision during Miocene subduction causes uplift along crustal-scale reverse faults in Fiordland, New Zealand. GSA Today, 29, 4–10.

Kula, J., Tulloch, A., Spell, T.L., and Wells, M.L. (2007) Two-stage rifting of Zealandia-Australia-Antarctica: Evidence from 40Ar/39Ar thermochronometry of the Sisters shear zone Stewart Island, New Zealand. Geology, 35, 411–414, doi: 10 .1130 /G23432A .1.

Lackey, J.S., Valley, J.W., and Saleeby, J.B. (2005) Supracrustal input to magmas in the deep crust of Sierra Nevada batholith: Evidence from high-$\delta^{18}O$ zircon. Earth and Planetary Science Letters, 235, 315–330.

Lackey, J.S., Valley, J.W., Chen, J.H., and Stockli, D.F. (2008) Dynamic magma systems, crustal recycling, and alteration in the Central Sierra Nevada batholith: The oxygen isotope record. Journal of Petrology, 49, 1397–1426.

Lackey, J.S., Cecil, M.R., Windham, C.J., Frazer, R.E., Bindeman, I.N., and Gehrels, G.E. (2012) The Fine Gold Intrusive Suite: The roles of basement terranes and magma source development in the Early Cretaceous Sierra Nevada batholith. Geosphere, 8, 292–313.

Landis, C.A., and Coombs, D.S. (1967) Metamorphic belts and orogenesis in southern New Zealand. Tectonophysics, 4, 501–518.

Lindquist, P. C. (2020) The architecture of a lower-crustal shear zone and evidence for along-strike variations in strain localization and partitioning, Fiordland, New Zealand. Graduate College Dissertations and Theses. https://scholarworks.uvm.edu/graddis/1260

Marcotte, S.B., Klepeis, K.A., Clarke, G.L., Gehrels, G.E., and Hollis, J.A. (2005) Intra-arc transpression in the lower crust and its relationship to magmatism in a Mesozoic magmatic arc. Tectonophysics, 407, 135–163.

McGinn, C., Miranda, E.A., and Hufford, L.J. (2020) The effects of quartz Dauphine twinning on strain localization in a mid-crustal shear zone. Journal of Structural Geology, 134, https://doi.org/10.1016/j.jsg.2020.103980

McCoy-West, A.J., Mortimer, N., and Ireland, T.R. (2014) U-Pb geochronology of Permian plutonic rocks, Longwood Range, New Zealand: Implications for Median Batholith-Brook Street Terrane relations. New Zealand Journal of Geology and Geophysics, 57, 65–85.

McCulloch, M.T., Bradshaw, J.Y., and Taylor, S.R. (1987) Sm-Nd and Rb-Sr isotope and geochemical systematics in Phanerozoic granulites from Fiordland, southwest New Zealand. Contributions to Mineralogy and Petrology, 97, 183–195.

Milan, L.A., Daczko, N.R., Clarke, G.L., and Allibone, A.H. (2016) Complexity of In-situ zircon U–Pb–Hf isotope systematics during arc magma genesis at the roots of a Cretaceous arc, Fiordland, New Zealand. Lithos, 264, 296–314.

Milan, L.A., Daczko, N.R., and Clarke, G.L. (2017) Cordillera Zealandia: A Mesozoic arc flare-up on the palaeo-Pacific Gondwana Margin. Scientific Reports, 7, 1–9.

Miller, J.S., Matzel, J.E.P., Miller, C.F., Burgess, S.D., and Miller, R.B. (2007) Zircon growth and recycling during the assembly of large, composite arc plutons. Journal of Volcanology and Geothermal Research, 167, 282–299.

Mortimer, N. (2004) New Zealand's Geological Foundations. Gondwana Research, 7, 261–272.

Mortimer, N., Tulloch, A.J., Spark, R.N., Walker, N.W., Ladley, E.B., Allibone, A.H., and Kimbrough, D.L. (1999) Overview of the Median Batholith, New Zealand: A new interpretation of the geology of the Median Tectonic Zone and adjacent rocks. Journal of African Earth Sciences, 29, 257–268.

Muir, R.J., Weaver, S.D., Bradshaw, J.D., Eby, G.N., and Evans, J.A. (1995) The Cretaceous Separation Point batholith, New Zealand: granitoid magmas formed by melting of mafic lithosphere. Journal of the Geological Society, 152, 689–701.

Muir, R.J., Ireland, T.R., Weaver, S.D., Bradshaw, J.D., Evans, J.A., Eby, G.N., and Shelley, D. (1998) Geochronology and geochemistry of a Mesozoic magmatic arc system, Fiordland, New Zealand. Journal of the Geological Society, 155, 1037–1053.

Nandedkar, R.H., Ulmer, P. & Müntener, O. (2014) Fractional crystallization of primitive, hydrous arc magmas: an experimental study at 0.7 GPa. Contributions to Mineralogy and Petrology. 167, 1015. https://doi.org/10.1007/s00410-014-1015-5

Park, S., Langmuir, C.H., Sims, K.W.W. et al. (2019) An isotopically distinct Zealandia–Antarctic mantle domain in the Southern Ocean. Nature Geoscience. 12, 206–214. https://doi.org/10.1038/s41561-018-0292-4

Paterson, S.R., and Ducea, M.N. (2015) Arc magmatic tempos: Gathering the evidence. Elements, 11, 91–98.

Petford, N. & Gallagher, K. (2001) Partial melting of mafic (amphibolitic) lower crust by periodic influx of basaltic magma. Earth and Planetary Science Letters, 193, 483–499.

Rudnick, R.L. (1995) Making continental crust. Nature, 378, 571–578, doi: 10.1038/378571a0.

Saleeby, J.B., Ducea, M.N., Busby, C.J., Nadin, E.S., and Wetmore, P.H. (2008) Chronology of pluton emplacement and regional deformation in the southern Sierra Nevada batholith, California. Geological Society of America Special Papers, 438, 397–427.

Sanderson, D.J., and Marchini, W.R.D. (1984) Transpression. Journal of Structural Geology, 6, 449–458.

Scholl, D.W., and Von Huene, R. (2007) Crustal recycling at modern subduction zones applied to the past-issues of growth and preservation of continental basement crust, mantle geochemistry, and supercontinent reconstruction. Geological Society of America Memoirs, 200, 9–32.

Schwartz, J.J., Stowell, H.H., Klepeis, K.A., Tulloch, A.J., Kylander-Clark, A.R.C., Hacker, B.R., and Coble, M.A. (2016) Thermochronology of extensional orogenic collapse in the deep crust of Zealandia. Geosphere, 12, 647–677.

Schwartz, J.J., Klepeis, K.A., Sadorski, J.F., Stowell, H.H., Tulloch, A.J., and Coble, M.A. (2017) The tempo of continental arc construction in the Mesozoic Median Batholith, Fiordland, New Zealand. Lithosphere, 9, 343–365.

Scott, J.M. (2013) A review of the location and significance of the boundary between the Western Province and Eastern Province, New Zealand. New Zealand Journal of Geology and Geophysics, 56, 276–293.

Scott, J.M., and Palin, J.M. (2008) LA-ICP-MS U-Pb zircon ages from Mesozoic plutonic rocks in eastern Fiordland, New Zealand. New Zealand Journal of Geology and Geophysics, 51, 105–113.

Scott, J.M., Cooper, A.F., Palin, J.M., Tulloch, A.J., Kula, J., Jongens, R., Spell, T.L., and Pearson, N.J. (2009) Tracking the influence of a continental margin on growth of a magmatic arc, Fiordland, New Zealand, using thermobarometry, thermochronology, and zircon U-Pb and Hf isotopes. Tectonics, 8, 1–20.

Scott, J.M., Cooper, A.F., Tulloch, A.J., and Spell, T.L. (2011) Crustal thickening of the Early Cretaceous paleo-Pacific Gondwana margin. Gondwana Research, 20, 380–394.

Sláma, J., Košler, J., Condon, D.J., Crowley, J.L., Gerdes, A., Hanchar, J.M., Horstwood, M.S.A., Morris, G.A., Nasdala, L., Norberg, N., and others (2008) Plešovice zircon - A new natural reference material for U-Pb and Hf isotope microanalysis. Chemical Geology, 249, 1–35.

Solano, J.M.S., Jackson, M.D., Sparks, R.S.J., Blundy, J.D., and Annen, C. (2012) Melt segregation in Deep Crustal Hot Zones: A Mechanism for Chemical Differentiation, Crustal Assimilation and the Formation of Evolved Magmas. Journal of Petrology, 53, 1999–2026.

Taylor, S.R., and McLennan, S.M. (1995) The geochemical evolution of the continental crust. Reviews of Geophysics, 33, 241–265, doi: 10.1029/95RG00262.

Thorkelson, D.J. (1996) Subduction of diverging plates and the principles of slab window formation. Tectonophysics, 255, 47–63.

Tulloch, A.J., and Kimbrough, D.L. (2003) Paired plutonic belts in convergent margins and the development of high Sr/Y magmatism: Peninsular Ranges batholith of Baja-California and Median batholith of New Zealand. Geological Society of America Special Papers, 374, 275–295.

Tulloch, A.J., Kimbrough, D.L., Landis, C.A., Mortimer, N., and Johnston, M.R. (1999) Relationships between the brook street Terrane and Median Tectonic Zone (Median Batholith): Evidence from Jurassic conglomerates. New Zealand Journal of Geology and Geophysics, 42, 279–293.

Tulloch, A.J., Ramezani, J., Kimbrough, D.L., Faure, K., and Allibone, A.H. (2009a) U-Pb geochronology of mid-Paleozoic plutonism in western New Zealand: Implications for S-type granite generation and growth of the east Gondwana margin. Geological Society of America Bulletin, 121, 1236–1261.

Tulloch, A.J., Ramezani, J., Mortimer, N., Mortensen, J., van den Bogaard, P., and Maas, R., (2009b) Cretaceous felsic volcanism in New Zealand and Lord Howe Rise (Zealandia) as a precursor to final Gondwana break-up, in Ring, U., and Wernicke, B., eds., Extending a

Continent: Architecture, Rheology and Heat Budget: Geological Society, London, Special Publication 321, 89–118, doi: 10 .1144 /SP321 .5 .

Turnbull R, Schwartz J, Fiorentini M, Jongens R, Ludwig T, Evans N, McDonald B & Klepeis K (2020) Mapping the 4D Lithospheric Architecture of Zealandia Using Zircon O and Hf Isotopes in Plutonic Rocks, Goldschmidt Abstracts, 2637.

Ulmer, P., Kaegi, R. & Müntener, O. (2018) Experimentally Derived Intermediate to Silica-rich Arc Magmas by Fractional and Equilibrium Crystallization at 1·0 GPa: an Evaluation of Phase Relationships, Compositions, Liquid Lines of Descent and Oxygen Fugacity. Journal of Petrology, 59, 11–58, https://doi.org/10.1093/petrology/egy017

Valley, J.W. (2003) Oxygen Isotopes in Zircon. Reviews in Mineralogy and Geochemistry, 53, 343–385.

Valley, J.W., Kinny, P.D., Schulze, D.J., and Spicuzza, M.J. (1998) Zircon megacrysts from kimberlite: Oxygen isotope variability among mantle melts. Contributions to Mineralogy and Petrology, 133, 1–11.

Valley, J.W., Bindeman, I.N., and Peck, W.H. (2003) Empirical calibration of oxygen isotope fractionation in zircon. Geochimica et Cosmochimica Acta, 67, 3257–3266.

Vervoort, J.D., and Blichert-Toft, J. (1999) Evolution of the depleted mantle: Hf isotope evidence from juvenile rocks through time. Geochimica et Cosmochimica Acta, 63, 533–556.

Vervoort, J.D., Patchett, P.J., Söderlund, U., and Baker, M. (2004) Isotope composition of Yb and the determination of Lu concentrations and Lu/Hf ratios by isotope dilution using MC-ICPMS. Geochemistry, Geophysics, Geosystems, 5, 1–15.

Voice, P.J., Kowalewski, M., and Eriksson, K.A. (2011) Quantifying the timing and rate of crustal evolution: Global compilation of radiometrically dated detrital zircon grains. Journal of Geology, 119, 109–126.

Waight, T.E., Weaver, S.D., and Muir, R.J. (1998) Mid-Cretaceous granitic magmatism during the transition from subduction to extension in southern New Zealand: a chemical and tectonic synthesis. Lithos, 45, 469–482.

Walker, B. A., Bergantz, G. W., Otamendi, J. E., Ducea, M. N. & Cristofolini, E. A. (2015) A MASH zone revealed: The mafic complex of the Sierra Valle Fértil. Journal of Petrology, 56, 1863–1896.

Wang X.-L., Coble M.A., Valley J.W., Shu X.-J.., Kitajima K, Spicuzza M.J., Sun T. (2014) Influence of radiation damage on late Jurassic zircon from southern China: Evidence from in situ measurement of oxygen isotopes, laser Raman, U-Pb ages, and trace elements. Chemical Geology, 389, 122-136.

Woodhead, J.D., and Hergt, J.M. (2005) A Preliminary Appraisal of Seven Natural Zircon Reference Materials for In Situ Hf Isotope Determination. Geostandards and Geoanalytical Research, 29, 183–195.

Zheng, Y.F., Wu, Y.B., Chen, F.K., Gong, B., Li, L., and Zhao, Z.F. (2004) Zircon U-Pb and oxygen isotope evidence for a large-scale ^{18}O depletion event in igneous rocks during the Neoproterozoic. Geochimica et Cosmochimica Acta, 68, 4145–4165.

Figure Captions

Figure 1. **A.** Simplified geologic map of Fiordland, New Zealand showing sample locations (white dots). Shear zones referenced in this study are shown in yellow, and include George Sound Shear Zone, Grebe Shear Zone, and Indecision Creek Shear Zone. These latter two faults divide the inboard and outboard Median Batholith. Map is modified from Ramezani and Tulloch (2009a). **B.** Inset map shows underlying basement terranes of present-day New Zealand. Dashed lines are extrapolations of terrane contacts. Line a-a' refers to cross-section in Fig. 1F. Figure adapted from Coombs et al. (1976). **C and D**. Simplified geologic map of Lake Te Anau (C) and Lake Manapouri area (D) and sample locations. **F**. Simplified reconstructed cross-section of Zealandia Cordillera prior to termination of arc magmatism. Modified after Mortimer et al. (2014). EP = Eastern Province; WP = Western Province; T. = Terrane; GSZ = Grebe Shear Zone; ICSZ = Indecision Creek Shear Zone; GSSZ = George Sound Shear Zone; OB = Outboard Median Batholith; IB = Inboard Median Batholith.

Figure 2. Blue-rock geochemical plots of Darran Suite, Separation Point Suite (SPS), and Western Fiordland Orthogneiss (WFO). The green field represents WFO samples from Decker et al. (2017). **A.** Classification of plutonic rocks based on SiO_2 and Na_2O+K_2O content, following Delavari et al. (2014); **B.** Shand's Index (Maniar and Piccoli, 1989); **C.** Modified alkali lime index versus SiO_2 (Frost et al., 2001); **D.** Fe-number versus SiO_2 (Frost et al., 2001).

Figure 3. Cathodoluminescence (CL) images of representative zircon and their analytical spots. Zircons display oscillatory and sector zoning consistent with magmatic growth. U-Pb spots (white circle), O spots (blue circle), and Hf spots (red circle) are shown where analysis occurred.

For each sample, a white 100-micron bar is shown for scale. Data for all spots can be found in Supplementary Tables 2-3.

Figure 4. Individual transect isotope data. $\delta^{18}O$ and initial ε_{Hf} zircon data from each arc-perpendicular transect are plotted against distance from the Grebe Shear Zone (GSZ)–Indecision Creek Shear Zone (ICSZ) and extension thereof (ext.). The western yellow bar marks the George Sound Shear Zone (GSSZ) and southern projection (proj.). Shear zone thicknesses are demarcated by thickness of the yellow bars. Transect locations are outlined on **Figure 1**. WID = Western Isotope Domain; CID = Central Isotope Domain; EID = Eastern Isotope Domain.

Figure 5. Combined isotope data relative to the Grebe Shear Zone–Indecision Creek Shear Zone. Yellow vertical bars show thicknesses of shear zone widths. **A.** $\delta^{18}O$ (Zrn) data vs. distance from the Grebe Shear Zone (GSZ). **B.** Initial ε_{Hf} (Zrn) data vs distance from the GSZ. WID = Western Isotope Domain; CID = Central Isotope Domain; EID = Eastern Isotope Domain.

Figure 6. Isotope Contour Plots for the Median Batholith. Sample locations are plotted as black dots. Ductile shear zones, outlined in a dark grey field, separate the three isotope domains. The George Sound Shear Zone and southern projection separate the WID and CID, and the Grebe Shear Zone–Indecision Creek Shear Zone separate the CID from the EID. Sample transects from **Figure 1** are outlined in black lines with associated transect letters. Oxygen isotope values increase from east to west (left), and hafnium isotope values increase from west to east (right). GSSZ = George Sound Shear Zone; GSSZ Proj. = Southern projection of the George Sound

Shear Zone; GSZ = Grebe Shear Zone; ICSZ = Indecision Creek Shear Zone; WID = Western Isotope Domain; CID = Central Isotope Domain; EID = Eastern Isotope Domain.

Figure 7. A. Zircon O-isotope contour plot in Lake Te Anau and Lake Manapouri showing pre-Cretaceous zircon sample locations and $^{206}Pb/^{238}U$ zircon ages. **B.** Zircon age vs. $\delta^{18}O$ (Zrn) for pre-Cretaceous samples. Existence of the isotope gradient in pre-Cretaceous samples indicates that the isotope in both the EID and CID gradient pre-dates Early Cretaceous transpression and contraction in the region and was therefore not caused by an Early Cretaceous tectonic event.

Figure 8. A. Block model of present-day locations of plutons from the Median Batholith and crustal architecture of the Eastern and Western provinces at depth. The George Sound Shear Zone separates the WID and CID, and demarcates the boundary of the underlying Eastern Province terrane. The Grebe Shear Zone – Indecision Creek Shear Zone separates the CID and EID, divides the inboard and outboard Median Batholith, and is the suture that separates the Eastern and Western Provinces. Graphs of oxygen (**B**) and hafnium (**C**) isotope trends are plotted against distance. WAL= West Arm Leucogranite, RO= Refrigerator Orthogneiss, Ptk=Puteketeke Pluton, ICC=Indecision Creek Complex, NF=North Fork Pluton, SZ=shear zone.

Figure 9. A. Zircon age vs. distance from GSZ (km). Low-Sr/Y, Darran Suite magmatism was focused within a 10-15 km zone relative to the Grebe Shear Zone–Indecision Creek Shear Zone system for >100 Myr from ca. 240 to 130 Ma. Emplacement of high-Sr/Y, Separation Point Suite

magmas is shown to have migrated continentward from 129-114 Ma at a rate of ~4-5 km/Myr. Distance from the GSZ (km) is measured from location shown in **Figure 1**.

Figure 10. A. Zircon oxygen-isotope values vs. zircon age (Ma). B. Zircon initial εHf values vs. zircon age (Ma).

Figure 11. Assimilation Fractional Crystallization (AFC) models for the WID (A), CID (B) and EID (C). Data illustrate the generation of WFO-like melts from recycling of trench sediments (A) and the assimilation of low-$\delta^{18}O$ crust by WFO-like melts in the CID and EID (B and C).

This is the peer-reviewed, final accepted version for American Mineralogist, published by the Mineralogical Society of America.
The published version is subject to change. Cite as Authors (Year) Title. American Mineralogist, in press.
DOI: https://doi.org/10.2138/am-2021-7626. http://www.minsocam.org/

List of Tables

Table 1. Terminology and subdivisions of the Median batholith. [1]Allibone et al. (2009a), Scott et al. (2009); [2]Scott (2013); [3]this study. GSSZ=George Sound shear zone; GSZ/ICSZ=Grebe shear zone/Indecision Creek shear zone. WID=Western Isotope Domain; CID=Central Isotope Domain; EID=Eastern Isotope Domain.

Table 2. Summary of zircon age, O- and Hf-isotope data for the Median Batholith.

Appendix Files

Supplementary Table 1. Bulk-rock XRF geochemistry.

Supplementary Table 2. Zircon Oxygen isotope data.

Supplementary Table 3. Zircon Lu-Hf isotope data.

Supplementary Figure 1. Secondary Hf zircon standard data.

Supplementary Figure 2. Hf stable isotope data for analyzed zircons.

Table 1. Terminology and Subdivisions of the Median Ba

West

Geographic Subdivision	Western Fiordland	George Sound Shear Zone
Batholith Subdivision	Inboard Median Batholith	
Terrane Subdivision	Takaka Terrane	
Spatial Isotope Domain	Western (WID)	
Defining Plutons	Separation Point Suite Western Fiordland Orthogneiss Darran Suite None recognized	

tholith

East

Central Fiordland	Grebe-Indecision Creek Shear Zone	Eastern Fiordland
Inboard Median Batholith		Outboard Median Batholith
Takaka Terrane		Drumduan Terrane
Central (CID)		Eastern (EID)
Separation Point Suite Puteketeke Pluton Refrigerator Orthogneiss West Arm Leucogranite Darran Suite Hunter Intrusives Murchison Intrusives		Separation Point Suite Takahe Granodiorite Titiroa Granodiorite North Fiord Granite Darran Suite Hunter Intrusives Murchison Intrusives

Table 2. Summary of zircon error-weighted average $^{206}Pb/^{238}U$ ages, O and Lu-Hf isotope data, Fiordland, New Zealand

Pluton	Sample Number	Age	$\delta^{18}O$ (Zrn) Mean ± 2SD	δ18O (Zrn) Range (‰)	n	Zrn Initial εHf ± 2SD	Zrn Initial εHf range	n	Reference
Breaksea Orthogneiss	13NZ33E	123.5 ± 1.4	5.30 ± 0.23	5.2 - 5.4	6	4.8 ± 3.5	6.5 - 2.7	20	2
Darran Leucogranite	OU49127	135.8 ± 2.3	3.97 ± 0.32	3.7 - 4.0	9	8.4 ± 3.2	9.4 - 6.0	20	3
Devils Armchair Pluton	15NZ66	133.4 ± 2.1	4.63 ± 0.35	4.0 - 5.3	8	5.4 ± 3.3	8.5 - (-)4.9	19	3
Eastern McKerr Intrusives	15NZ12	128.3 ± 3.9	-5.83 ± 0.30	(-)7.4 - 0.4	8	2.6 ± 3.1	5.2 - (-)0.2	17	2,3
Eastern McKerr Intrusives	15NZ20	118.8 ± 2.8	5.77 ± 0.27	5.5 - 6.0	6	3.8 ± 3.1	5.7 - -2.0	20	2
Glade Suite	OU49129	140.6 ± 1.5	4.06 ± 0.30	3.8 - 4.1	7	7.9 ± 3.1	10.0 - 5.9	20	3
Hunter Intrusives	17NZ46	351.5 ± 9.9	4.83 ± 0.27	5.0 - 4.7	7	n.d.	n.d.	n.d.	1
Hunter Intrusives	17NZ65A	156.0 ± 1.7	4.18 ± 0.12	4.2 - 4.1	7	9.6 ± 1.2	10.5 - 8.2	10	1
Hunter Intrusives	17NZ72A	143.4 ± 4.4	3.81 ± 0.44	4.2 - 3.6	5	7.5 ± 1.3	8.4 - 6.4	6	1
Hunter Intrusives	17NZ87	156.0 ± 1.7	4.80 ± 0.18	5.0 - 4.7	7	7.9 ± 1.7	9.0 - 6.7	12	1
Hunter Intrusives	OU49100	169.0 ± 3.1	4.91 ± 0.22	4.1 - 5.2	12	7.9 ± 3.3	11.1 - 5.2	20	3
Hunter Intrusives	OU49102	149.6 ± 1.6	4.36 ± 0.30	4.2 - 4.5	8	7.8 ± 3.3	10.1 - 3.7	20	3
Malaspina Pluton	12DC41C	115.9 ± 1.2	5.74 ± 0.19	5.6 - 5.9	8	n.d.	n.d.	n.d.	1
Malaspina Pluton	13NZ11	n.d.	5.80 ± 0.35	6.0 - 5.6	5	n.d.	n.d.	n.d.	1
Malaspina Pluton	13NZ14	n.d.	5.82 ± 0.17	5.7 - 5.9	6	n.d.	n.d.	n.d.	1
Malaspina Pluton	13NZ16B	118.0 ± 2.1	5.74 ± 0.27	5.5 - 5.9	7	4.2 ± 3.1	5.6 - 2.1	20	2
Malaspina Pluton	13NZ22	116.9 ± 1.6	5.67 ± 0.37	5.5 - 5.9	5	4.2 ± 3.4	6.2 - 3.0	17	2
Malaspina Pluton	13NZ34A	118.0 ± 1.8	5.74 ± 0.39	5.5 - 6.0	7	2.9 ± 3.3	4.6 - 1.2	20	2
Malaspina Pluton	13NZ40D1	116.4 ± 1.3	5.74 ± 0.37	5.4 - 5.9	9	3.6 ± 3.3	5.3 - 1.9	17	2
Malaspina Pluton	13NZ59	117.5 ± 1.0	5.75 ± 0.27	5.7 - 5.8	6	4.3 ± 3.1	6.5 - 1.9	20	2
Malaspina Pluton	14NZ82	n.d.	5.72 ± 0.17	5.9 - 5.7	6	n.d.	n.d.	n.d.	1
Misty Pluton	12NZ22A	114.7 ± 1.1	5.68 ± 0.17	5.5 - 5.8	7	4.7 ± 3.4	10.8 - 1.3	20	2
Misty Pluton	12NZ24	115.8 ± 2.1	5.75 ± 0.12	5.6 - 6.0	6	3.9 ± 3.3	6.0 - 2.9	20	2
Misty Pluton	12NZ33	114.5 ± 2.1	5.56 ± 0.23	5.4 - 5.6	8	4 ± 3.6	5.7 - 2.0	20	2
Misty Pluton	12NZ36B	119.7 ± 1.3	5.78 ± 0.20	5.5 - 5.9	5	3.9 ± 3.4	4.9 - 2.8	20	2
Misty Pluton	13NZ46	116.9 ± 1.2	5.87 ± 0.17	5.6 - 6.0	8	4.4 ± 3.1	11.2 - 2.6	20	2,4
Misty Pluton	13NZ52A	116.8 ± 1.6	6.05 ± 0.38	5.8 - 6.2	5	3.9 ± 2.9	5.4 - 2.5	20	2
Misty Pluton	13NZ55A	115.2 ± 1.9	5.87 ± 0.40	5.7 - 6.1	7	4.4 ± 2.9	7.7 - 2.1	20	2
Misty Pluton	13NZ58	115.3 ± 1.5	6.06 ± 0.27	5.7 - 6.2	7	4.3 ± 2.9	5.4 - 1.4	20	2
Misty Pluton	P76640	117.89 ± 0.13	5.73 ± 0.19	5.9 - 5.6	8	n.d.	n.d.	n.d.	1
Misty Pluton	P76705	n.d.	5.72 ± 0.22	5.9 - 5.6	6	4.4 ± 1.2	5.2 - 3.7	7	1
Misty Pluton	P76709	ca. 116.4	5.89 ± 0.20	6.0 - 5.8	7	n.d.	n.d.	n.d.	1
Misty Pluton	P77630	118.42 ± 0.06	5.30 ± 0.32	5.2 - 5.6	5	n.d.	n.d.	n.d.	1,4
Misty Pluton	P77844	n.d.	4.76 ± 0.23	4.6 - 4.9	6	n.d.	n.d.	n.d.	1
Murchinson Intrusives	17NZ31A	133.5 ± 2.8	4.81 ± 0.44	5.0 - 4.4	5	n.d.	n.d.	n.d.	1
Murchinson Intrusives	17NZ40	170.0 ± 1.5	5.13 ± 0.24	5.0 - 5.3	10	7.9 ± 0.8	8.3 - 7.4	8	1
Nurse Suite	OU49128	140.8 ± 1.6	3.80 ± 0.28	3.4 - 4.1	6	n.d.	n.d.	n.d.	3
Omaki Orthogneiss	P75785	124.91 ± 0.17	4.75 ± 0.2	4.9 - 4.5	7	4.3 ± 0.6	4.7 - 3.9	7	1
Pembroke diorite	05NZ12P	134.2 ± 2.9	4.45 ± 0.28	4.2 - 4.5	8	8.2 ± 3.1	10.3 - 6.5	20	3
Pomona Island granite	OU49120	163.1 ± 1.8	3.90 ± 0.19	3.6 - 4.1	10	11.2 ± 3.4	17.9 - 5.7	20	3
Puteketeke Pluton	17NZ100	122.6 ± 1.4	4.98 ± 0.28	5.2 - 4.8	8	4.3 ± 1.4	5.2 - 3.2	10	1
Puteketeke Pluton	17NZ104	n.d.	4.88 ± 0.30	5.1 - 4.7	6	5.23 ± 2.0	7.0 - 3.8	8	1
Puteketeke Pluton	17NZ98	122.0 ± 1.6	4.79 ± 0.23	5.0 - 4.7	6	4.4 ± 1.3	5.6 - 3.6	10	1
Puteketeke Pluton	OU75705	120.8 ± 0.9	4.89 ± 0.30	5.1 - 4.7	10	4.5 ± 1.2	5.3 - 3.8	8	1
Puteketeke Pluton	P73900	n.d.	4.67 ± 0.15	4.8 - 4.6	7	4.4 ± 0.7	4.9 - 3.9	9	1
Refrigerator Orthogneiss	17NZ12	128.8 ± 1.7	4.67 ± 0.22	4.8 - 4.5	6	5.5 ± 1.6	6.6 - 4.2	9	1
Refrigerator Orthogneiss	17NZ124A	127.4 ± 1.3	5.10 ± 0.26	5.2 - 4.9	7	3.7 ± 0.5	3.9 - 3.4	7	1
Refrigerator Orthogneiss	17NZ25A	129.2 ± 1.7	4.74 ± 0.25	4.6 - 4.9	6	5.9 ± 1.0	6.8 - 5.5	8	1
Refrigerator Orthogneiss	OU75782	120.7 ± 1.1	5.31 ± 0.12	5.4 - 5.2	6	n.d.	n.d.	n.d.	1
Resolution Orthogneiss	12NZ12B	115.1 ± 2.1	5.85 ± 0.25	5.3 - 6.1	7	4.0 ± 3.2	7.9 - 2.2	20	2
Takahe Granodiorite	17NZ78B	125.1 ± 1.7	3.86 ± 0.21	4.0 - 3.8	6	7.6 ± 0.8	8.4 - 7.2	8	1
Takahe Granodiorite	17NZ81	123.2 ± 1.8	3.74 ± 0.26	4.0 - 3.6	7	7.1 ± 1.7	8.3 - 5.9	9	1
Titiroa Pluton	P69040	n.d.	3.83 ± 0.35	4.0 - 3.6	8	8.0 ± 0.8	8.5 - 7.5	8	1
West Arm Leucogranite	17NZ114	123.9 ± 1.5	5.39 ± 0.29	5.6 - 5.2	8	4.3 ± 0.6	4.7 - 3.8	7	1
West Arm Leucogranite	17NZ117	113.3 ± 1.6	5.88 ± 0.14	5.9 - 5.8	4	3.0 ± 8.4	8.8 - (-)0.8	4	1
West Arm Leucogranite	17NZ134	122.5 ± 1.8	5.26 ± 0.39	5.5 - 5.0	4	n.d.	n.d.	n.d.	1
West Arm Leucogranite	17NZ140	116.9 ± 1.8	5.68 ± 0.38	6.0 - 5.5	5	4.1 ± 2.5	5.5 - 0.1	11	1
Worsley Pluton	15NZ02	121.6 ± 1.9	5.46 ± 0.38	5.2 - 5.6	8	4.9 ± 3.3	6.9 - 3.5	20	2
Worsley Pluton	15NZ27	123.2 ± 1.9	5.95 ± 0.45	5.6 - 6.2	10	5.0 ± 3.1	6.1 - 2.6	20	2
Worsley Pluton	OU49144	119.3 ± 1.8	4.57 ± 0.17	4.8 - 4.5	6	5.5 ± 1.3	6.1 - 4.6	7	1

[1]this study
[2]Decker et al. (2017)
[3]Decker (2016)
[4]Tulloch, personal communication (2019)
[5]Ringwood and Schwartz. Unpublished data
[6]Buritica et al. (2019)

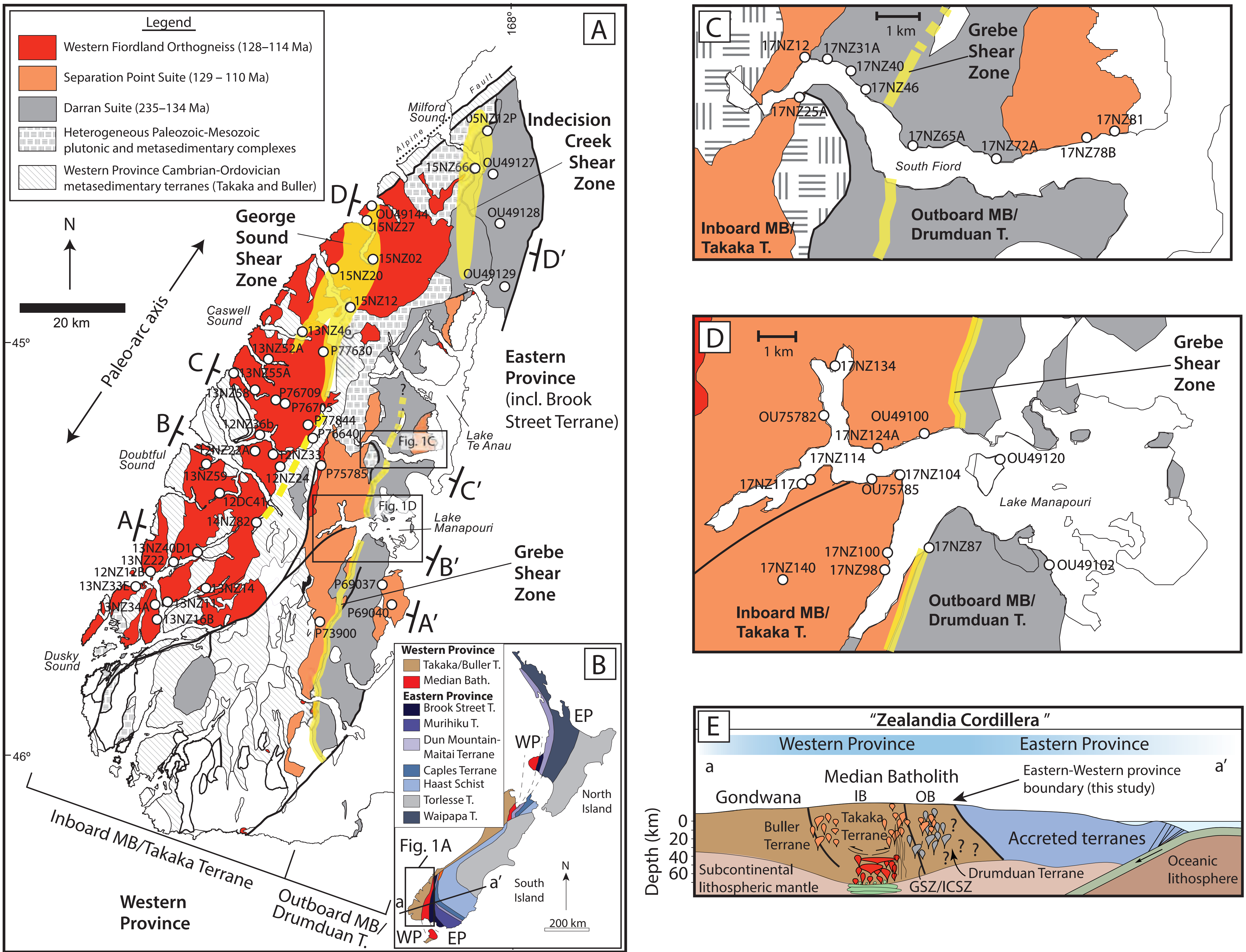
A
Legend
Western Fiordland Orthogneiss (128–114 Ma)
Separation Point Suite (129 – 110 Ma)
Darran Suite (235–134 Ma)
Heterogeneous Paleozoic-Mesozoic plutonic and metasedimentary complexes
Western Province Cambrian-Ordovician metasedimentary terranes (Takaka and Buller)
N
20 km
Paleo-arc axis
George Sound Shear Zone
Indecision Creek Shear Zone
Eastern Province (incl. Brook Street Terrane)
Grebe Shear Zone
Milford Sound
Alpine Fault
Caswell Sound
Doubtful Sound
Dusky Sound
Lake Te Anau
Lake Manapouri
Fig. 1C
Fig. 1D
45°
46°
168°
Inboard MB/Takaka Terrane
Outboard MB/ Drumduan T.
Western Province
B
Western Province
Takaka/Buller T.
Median Bath.
Eastern Province
Brook Street T.
Murihiku T.
Dun Mountain-Maitai Terrane
Caples Terrane
Haast Schist
Torlesse T.
Waipapa T.
Fig. 1A
WP
EP
North Island
South Island
200 km
C
1 km
Grebe Shear Zone
South Fiord
Inboard MB/ Takaka T.
Outboard MB/ Drumduan T.
D
1 km
Grebe Shear Zone
Lake Manapouri
Inboard MB/ Takaka T.
Outboard MB/ Drumduan T.
E
"Zealandia Cordillera"
Western Province
Eastern Province
a
a′
Median Batholith
Gondwana
IB
OB
Eastern-Western province boundary (this study)
Buller Terrane
Takaka Terrane
Accreted terranes
Depth (km)
Subcontinental lithospheric mantle
Drumduan Terrane
GSZ/ICSZ
Oceanic lithosphere

Figure 1

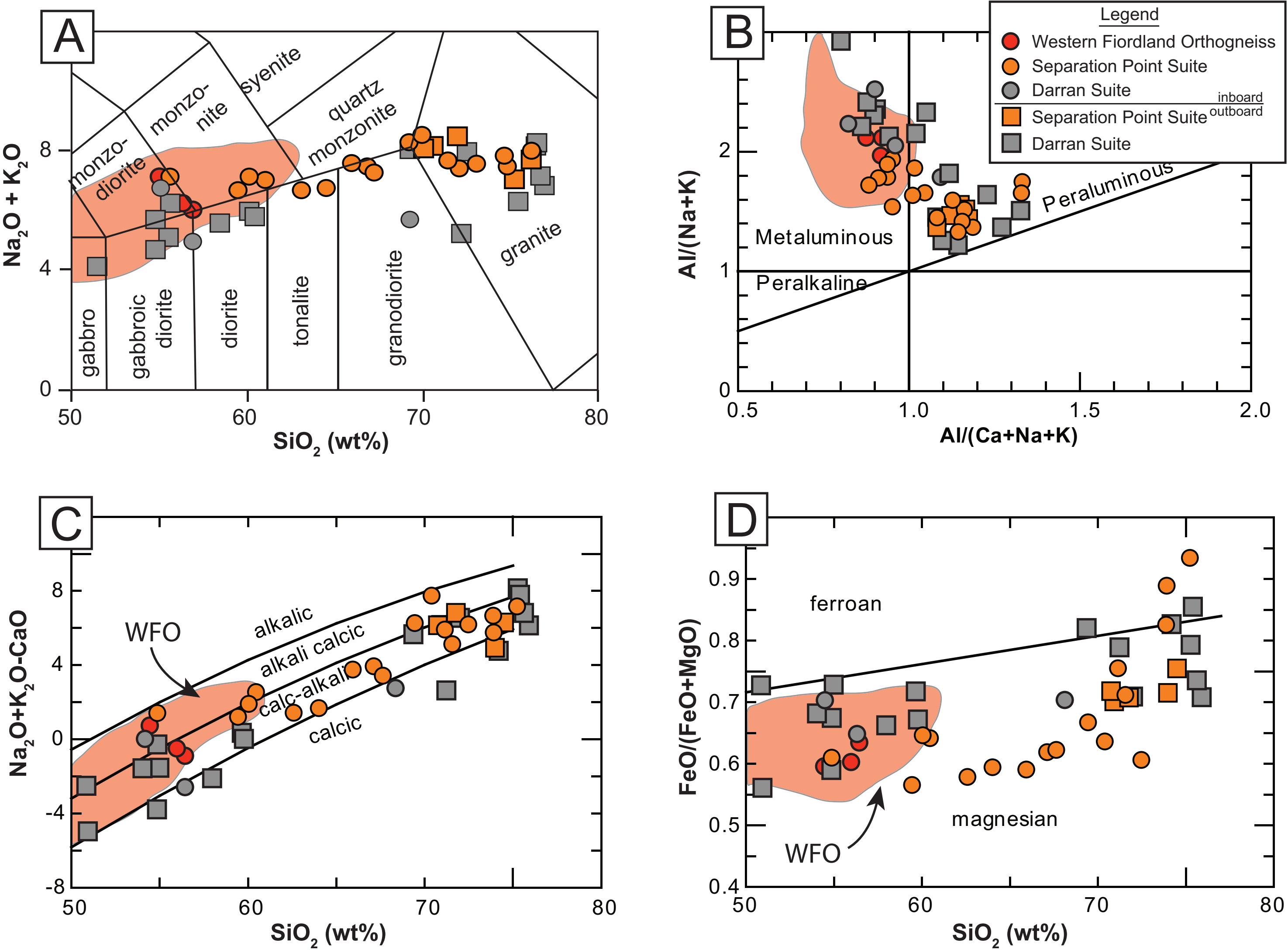

A
B
C
D
monzo-diorite
monzo-nite
syenite
quartz monzonite
granite
gabbro
gabbroic diorite
diorite
tonalite
granodiorite
Na2O + K2O
SiO2 (wt%)
Legend
Western Fiordland Orthogneiss
Separation Point Suite
Darran Suite
inboard
outboard
Separation Point Suite
Darran Suite
Metaluminous
Peralkaline
Peraluminous
Al/(Na+K)
Al/(Ca+Na+K)
WFO
alkalic
alkali calcic
calc-alkalic
calcic
Na2O+K2O-CaO
ferroan
magnesian
FeO/(FeO+MgO)

Figure 2

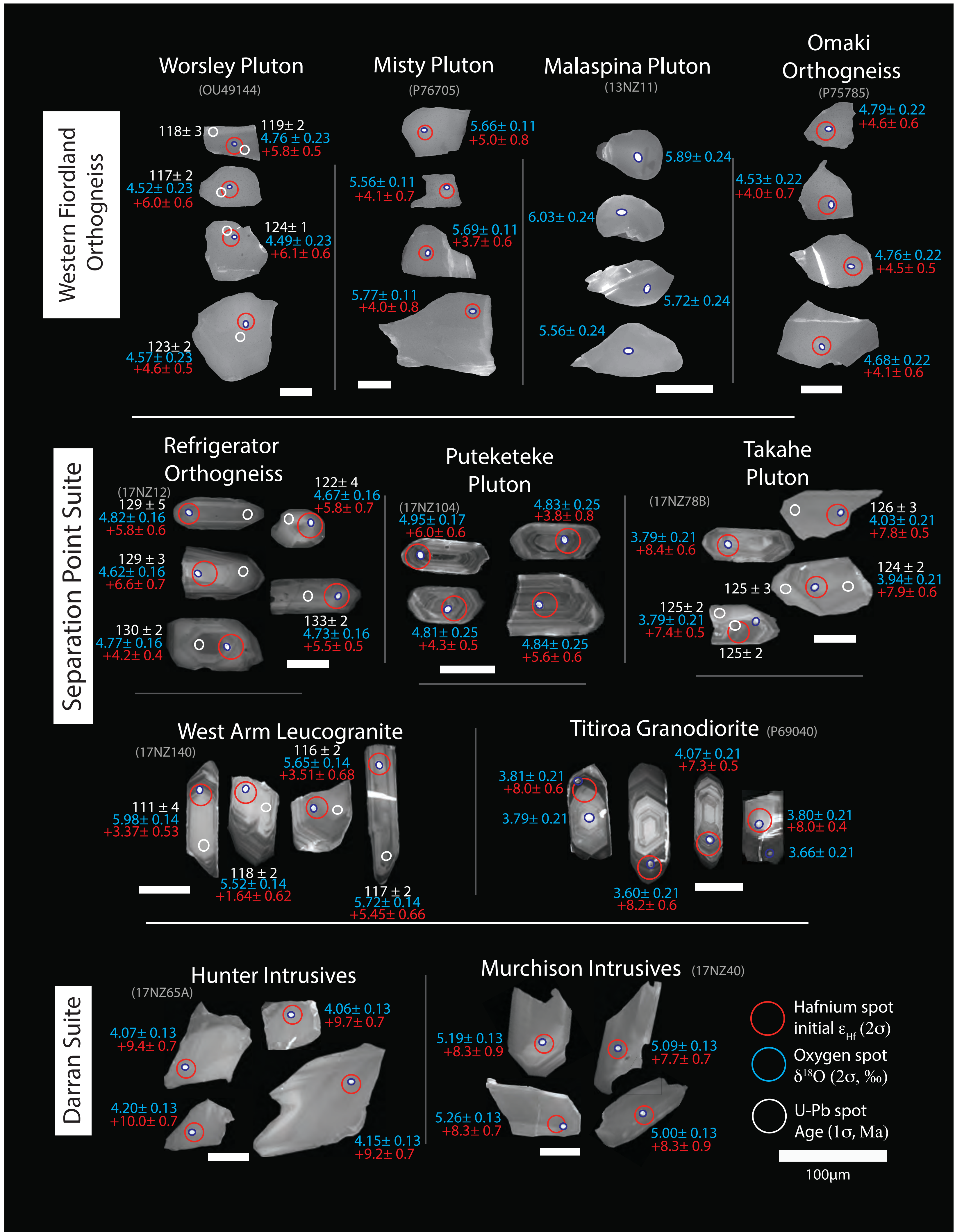

Western Fiordland Orthogneiss
Worsley Pluton
(OU49144)
Misty Pluton
(P76705)
Malaspina Pluton
(13NZ11)
Omaki Orthogneiss
(P75785)
Separation Point Suite
Refrigerator Orthogneiss
(17NZ12)
Puteketeke Pluton
(17NZ104)
Takahe Pluton
(17NZ78B)
West Arm Leucogranite
(17NZ140)
Titiroa Granodiorite (P69040)
Darran Suite
Hunter Intrusives
(17NZ65A)
Murchison Intrusives (17NZ40)
Hafnium spot initial ε$_{Hf}$ (2σ)
Oxygen spot δ^{18}O (2σ, ‰)
U-Pb spot Age (1σ, Ma)
100μm

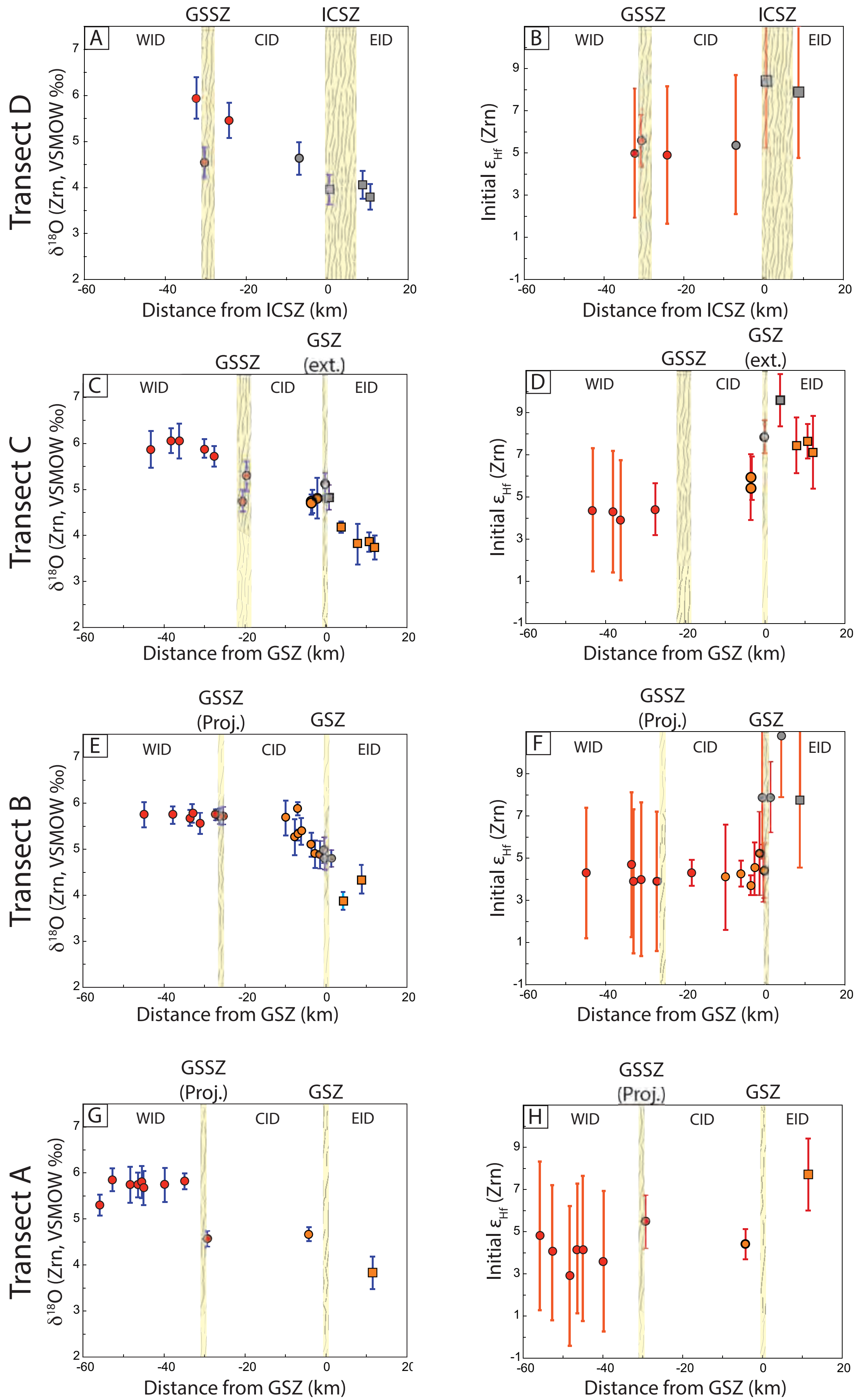
Transect D
Transect C
Transect B
Transect A
A
B
C
D
E
F
G
H
GSSZ
ICSZ
GSZ (ext.)
GSSZ (Proj.)
GSZ
WID
CID
EID
δ18O (Zrn, VSMOW ‰)
Initial εHf (Zrn)
Distance from ICSZ (km)
Distance from GSZ (km)

Figure 4

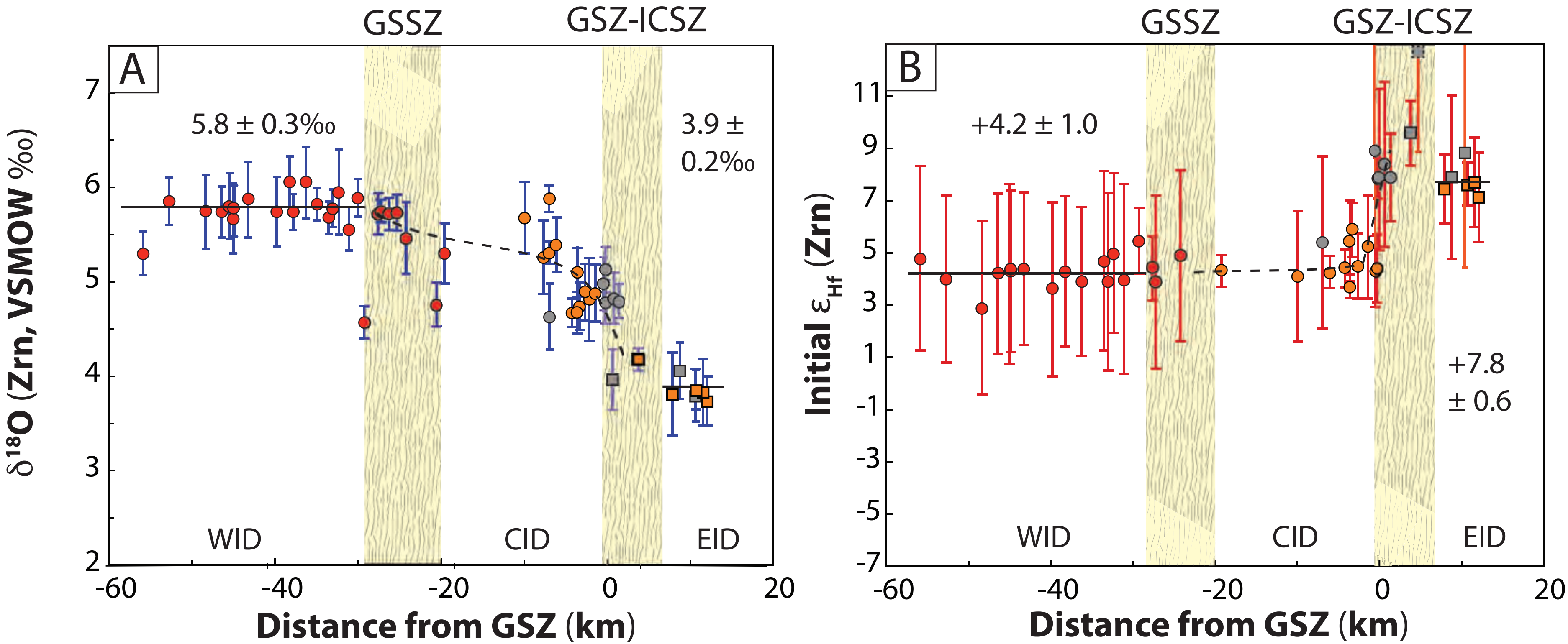
A
GSSZ
GSZ-ICSZ
5.8 ± 0.3‰
3.9 ± 0.2‰
WID
CID
EID
δ18O (Zrn, VSMOW ‰)
Distance from GSZ (km)
B
GSSZ
GSZ-ICSZ
+4.2 ± 1.0
+7.8 ± 0.6
WID
CID
EID
Initial εHf (Zrn)
Distance from GSZ (km)

Figure 5

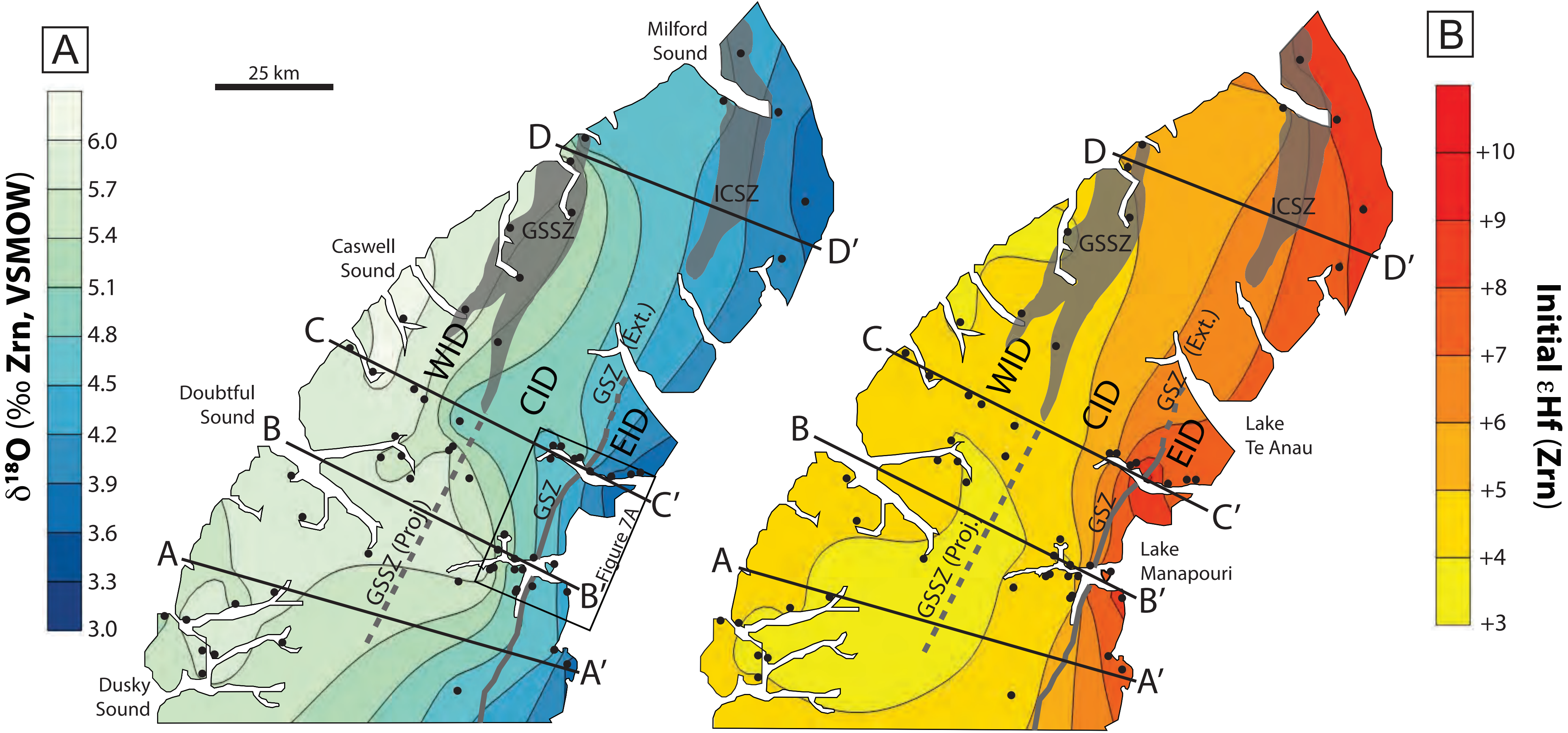
A
B
25 km
δ18O (‰ Zrn, VSMOW)
6.0
5.7
5.4
5.1
4.8
4.5
4.2
3.9
3.6
3.3
3.0
Initial εHf (Zrn)
+10
+9
+8
+7
+6
+5
+4
+3
Milford Sound
Caswell Sound
Doubtful Sound
Dusky Sound
Lake Te Anau
Lake Manapouri
A
A′
B
B′
C
C′
D
D′
ICSZ
GSSZ
WID
CID
EID
GSZ
GSZ (Ext.)
GSSZ (Proj.)
Figure 7A

Figure 6

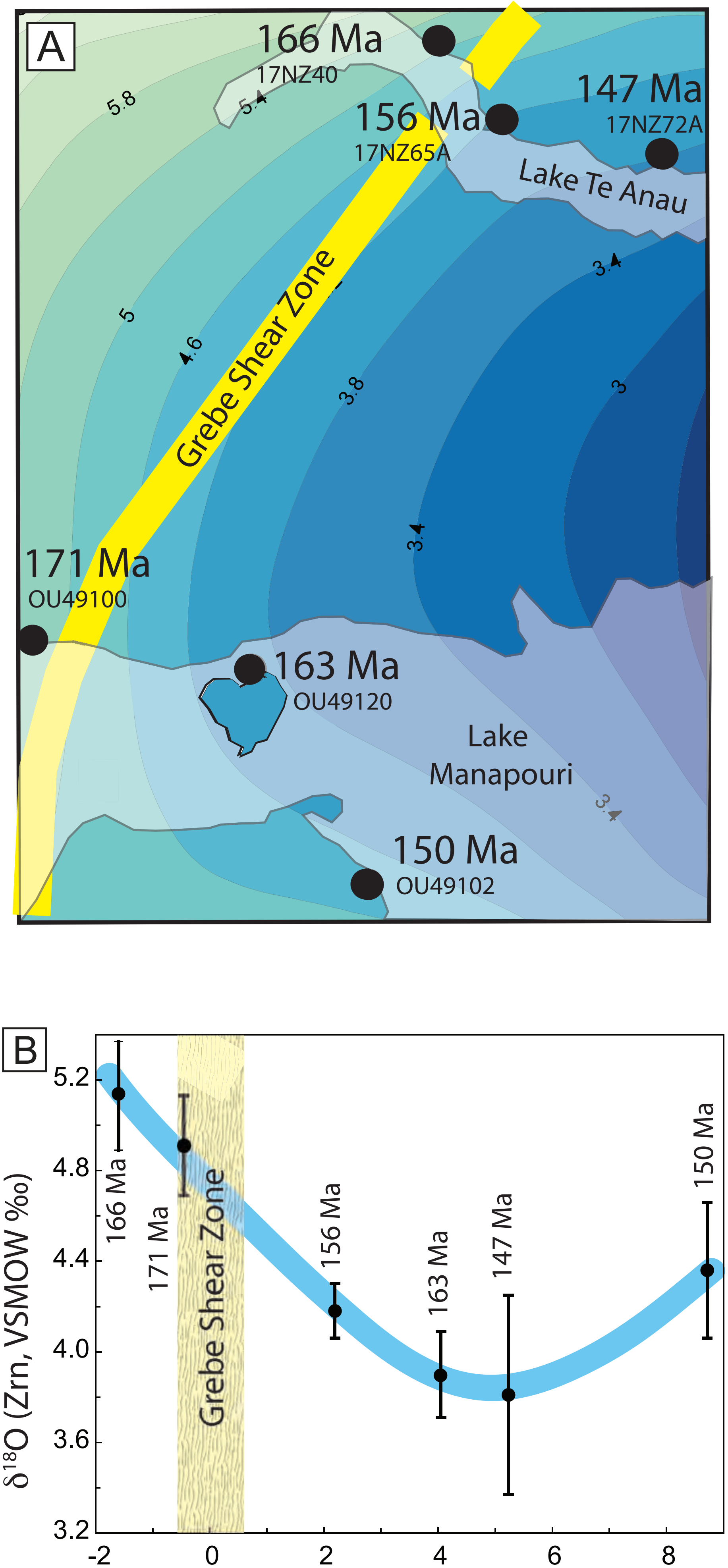
A
166 Ma
17NZ40
156 Ma
17NZ65A
147 Ma
17NZ72A
Lake Te Anau
Grebe Shear Zone
171 Ma
OU49100
163 Ma
OU49120
Lake
Manapouri
150 Ma
OU49102
5.8
5.4
5
4.6
3.8
3.4
3
B
δ18O (Zrn, VSMOW ‰)
Distance from GSZ (km)
166 Ma
171 Ma
Grebe Shear Zone
156 Ma
163 Ma
147 Ma
150 Ma
5.2
4.8
4.4
4.0
3.6
3.2
-2
0
2
4
6
8

Figure 7

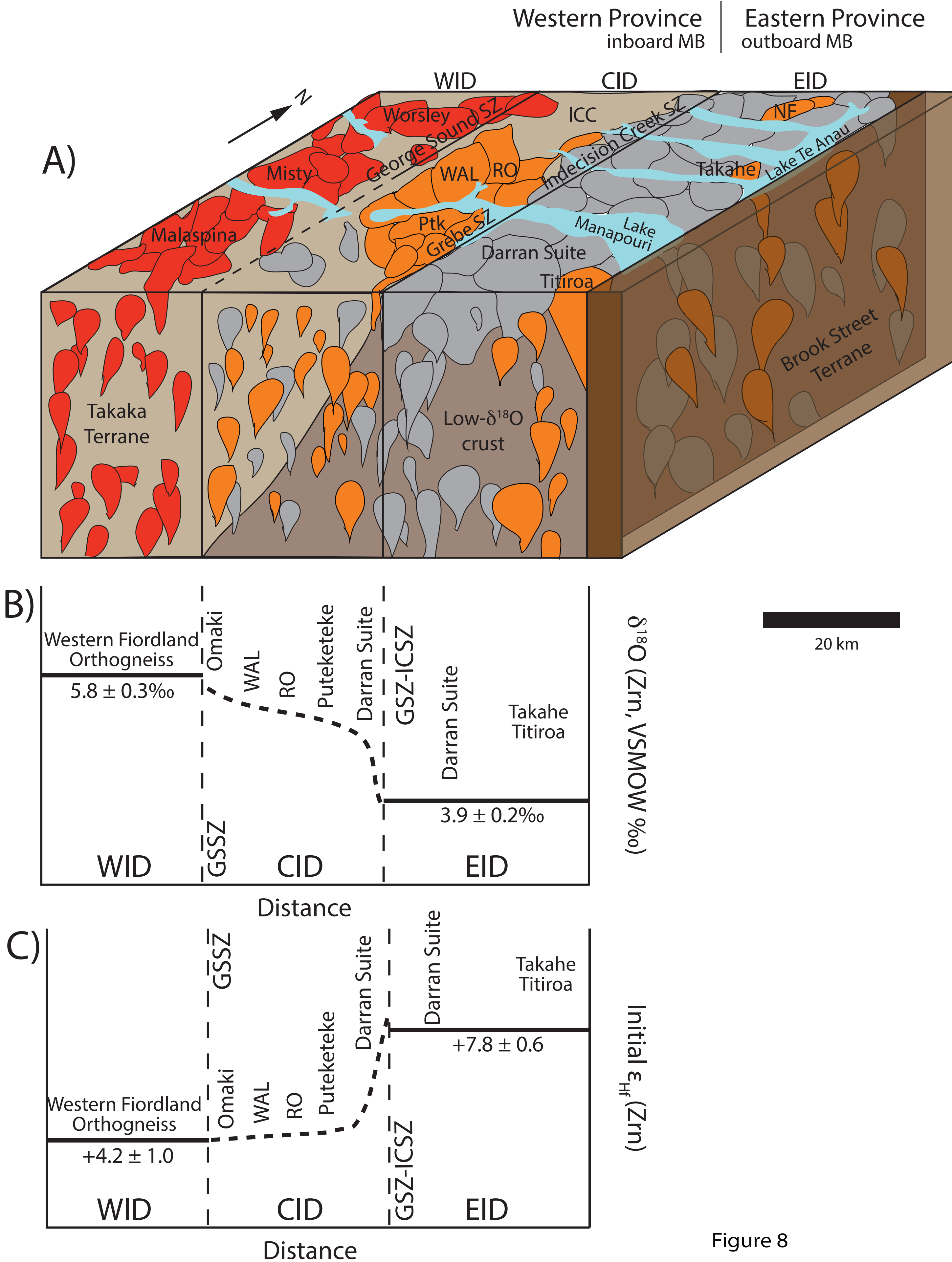

Western Province
inboard MB
Eastern Province
outboard MB
WID
CID
EID
N
A)
Worsley
George Sound SZ
ICC
Indecision Creek SZ
NF
Misty
WAL
RO
Takahe
Lake Te Anau
Malaspina
Ptk
Grebe SZ
Lake
Manapouri
Darran Suite
Titiroa
Takaka
Terrane
Low-δ18O
crust
Brook Street
Terrane
B)
Western Fiordland
Orthogneiss
5.8 ± 0.3‰
Omaki
WAL
RO
Puteketeke
Darran Suite
GSZ-ICSZ
Darran Suite
Takahe
Titiroa
3.9 ± 0.2‰
GSSZ
WID
CID
EID
Distance
δ18O (Zrn, VSMOW ‰)
20 km
C)
GSSZ
Darran Suite
Darran Suite
Takahe
Titiroa
+7.8 ± 0.6
Puteketeke
Western Fiordland
Orthogneiss
Omaki
WAL
RO
+4.2 ± 1.0
GSZ-ICSZ
WID
CID
EID
Distance
Initial εHf (Zrn)

Figure 8

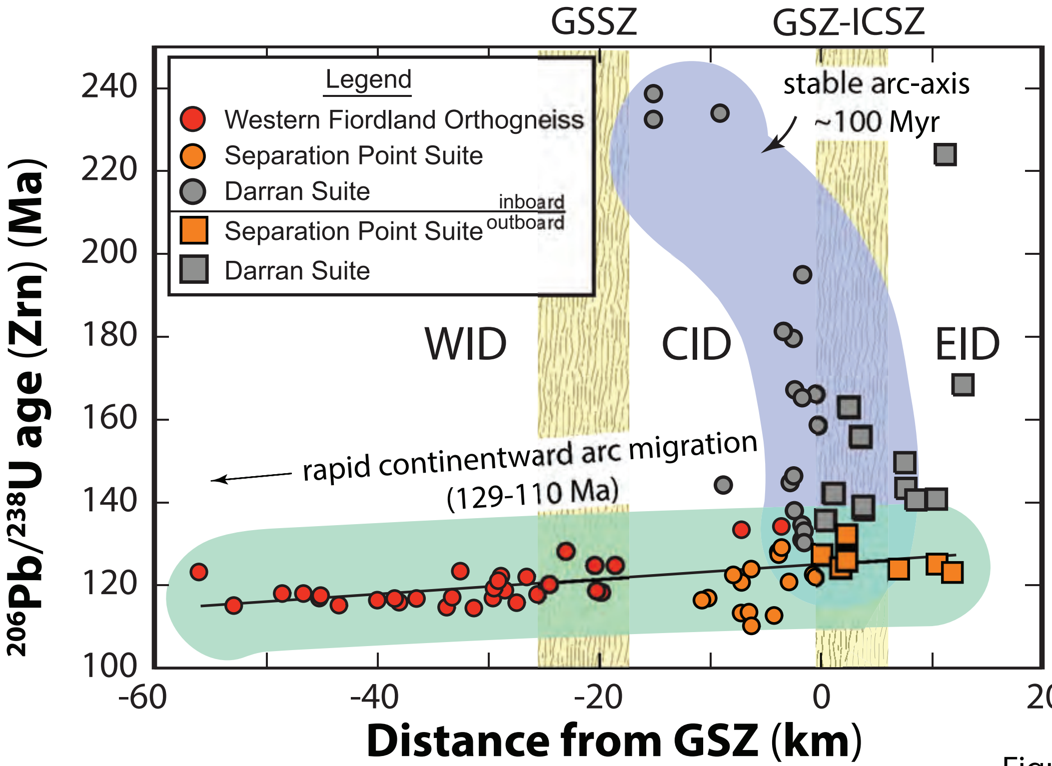

GSSZ
GSZ-ICSZ
Legend
Western Fiordland Orthogneiss
Separation Point Suite
Darran Suite
inboard
outboard
Separation Point Suite
Darran Suite
stable arc-axis
~100 Myr
WID
CID
EID
rapid continentward arc migration
(129-110 Ma)
240
220
200
180
160
140
120
100
-60
-40
-20
0
20
$^{206}Pb/^{238}U$ age (Zrn) (Ma)
Distance from GSZ (km)

Figure 9

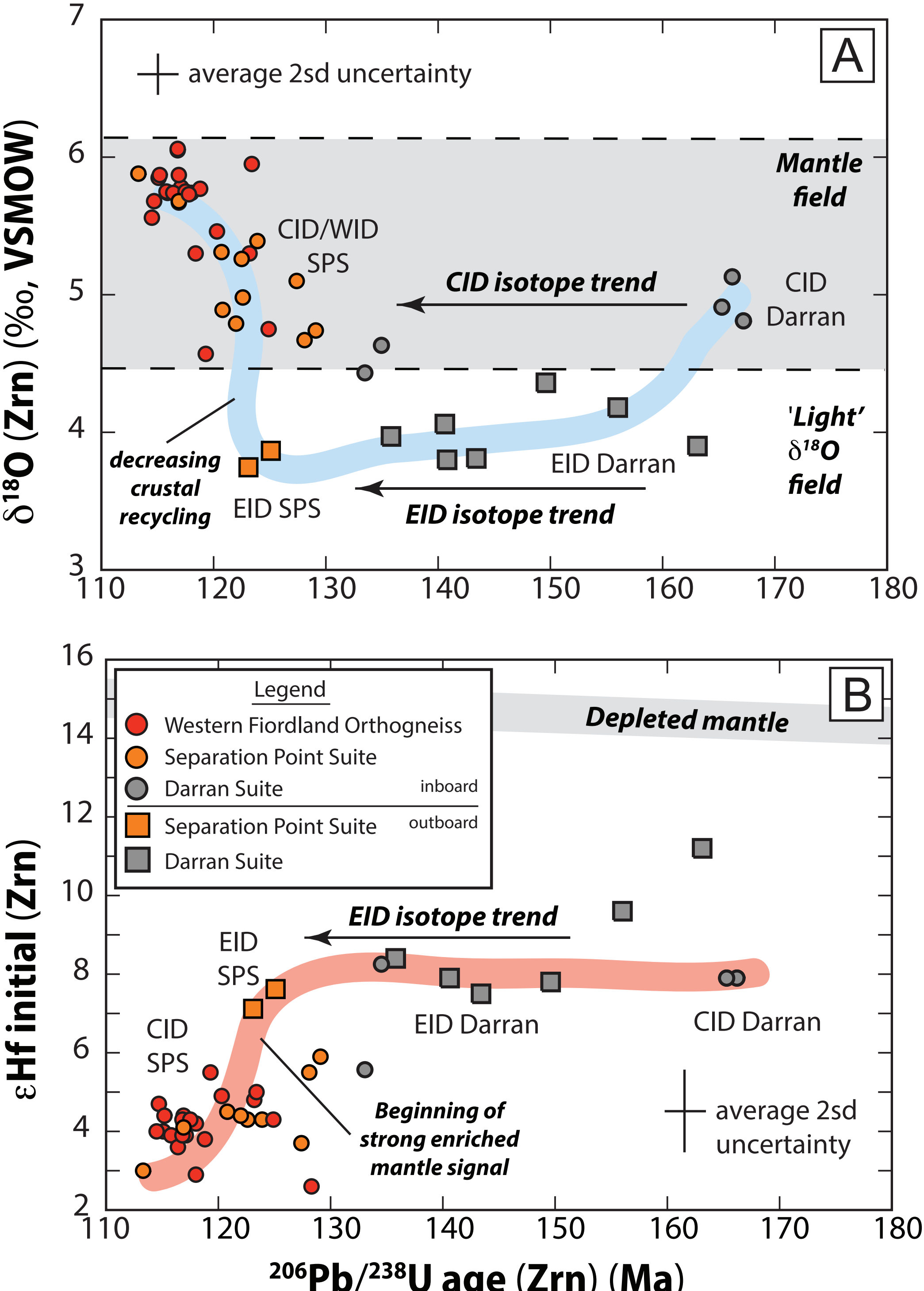
A
average 2sd uncertainty
Mantle field
CID/WID SPS
CID isotope trend
CID Darran
'Light' $\delta^{18}O$ field
decreasing crustal recycling
EID SPS
EID Darran
EID isotope trend
$\delta^{18}O$ (Zrn) (‰, VSMOW)
B
Legend
Western Fiordland Orthogneiss
Separation Point Suite
Darran Suite
inboard
Separation Point Suite
outboard
Darran Suite
Depleted mantle
EID isotope trend
EID SPS
CID SPS
EID Darran
CID Darran
Beginning of strong enriched mantle signal
average 2sd uncertainty
εHf initial (Zrn)
$^{206}Pb/^{238}U$ age (Zrn) (Ma)

Figure 10

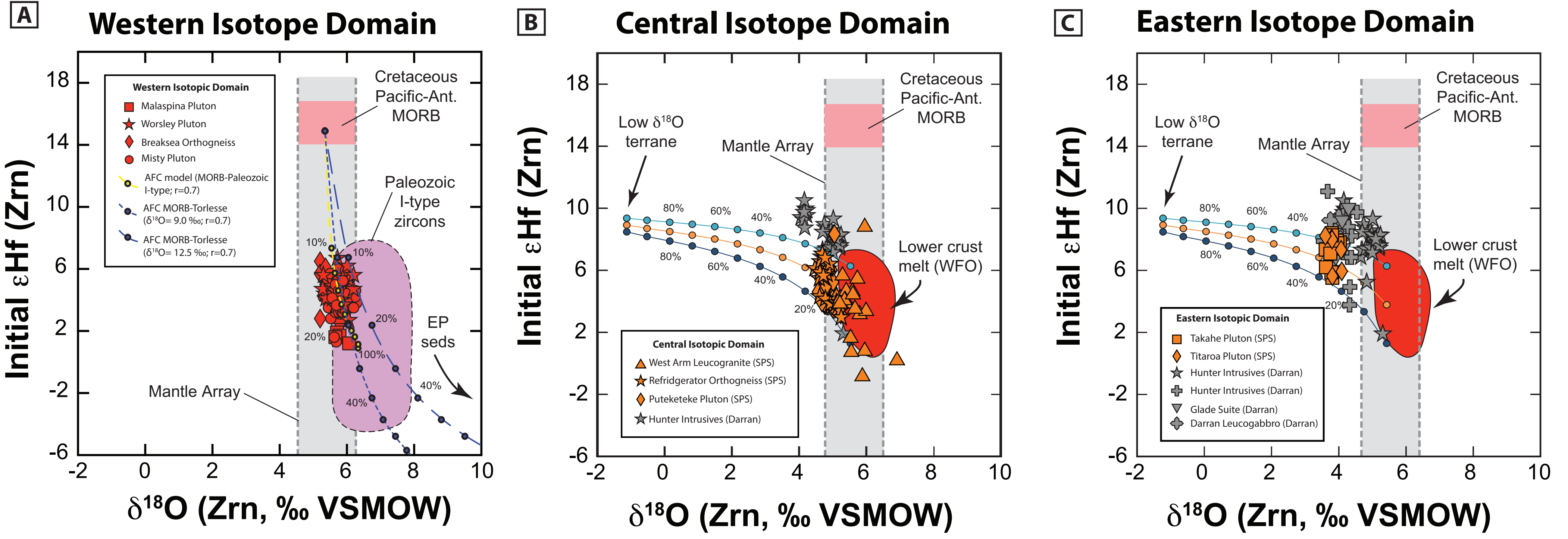
A
Western Isotope Domain
Western Isotopic Domain
Malaspina Pluton
Worsley Pluton
Breaksea Orthogneiss
Misty Pluton
AFC model (MORB-Paleozoic I-type; r=0.7)
AFC MORB-Torlesse (δ18O= 9.0 ‰; r=0.7)
AFC MORB-Torlesse (δ18O= 12.5 ‰; r=0.7)
Cretaceous Pacific-Ant. MORB
Paleozoic I-type zircons
EP seds
Mantle Array
B
Central Isotope Domain
Low δ18O terrane
Mantle Array
Cretaceous Pacific-Ant. MORB
Lower crust melt (WFO)
Central Isotopic Domain
West Arm Leucogranite (SPS)
Refridgerator Orthogneiss (SPS)
Puteketeke Pluton (SPS)
Hunter Intrusives (Darran)
C
Eastern Isotope Domain
Low δ18O terrane
Mantle Array
Cretaceous Pacific-Ant. MORB
Lower crust melt (WFO)
Eastern Isotopic Domain
Takahe Pluton (SPS)
Titaroa Pluton (SPS)
Hunter Intrusives (Darran)
Hunter Intrusives (Darran)
Glade Suite (Darran)
Darran Leucogabbro (Darran)
Initial εHf (Zrn)
δ18O (Zrn, ‰ VSMOW)

Figure 11